Development of a Robust Numerical Optimization Methodology for Turbine Endwalls and Effect of Endwall Contouring on Turbine Passage Performance

Kapil Vitthalbhai Panchal

Dissertation submitted to the faculty of the Virginia Polytechnic Institute and State University in partial fulfillment of the requirements for the degree of

Doctor of Philosophy

In

Mechanical Engineering

Srinath V. Ekkad, Co-Chair
Wing F. Ng, Co-Chair

Clinton L. Dancey
Mark A. Stremler
Danesh K. Tafti

October 7, 2011
Blacksburg, Virginia

Keywords: Gas Turbines, Endwall Contouring Optimization, Aerodynamics, Heat Transfer, Transonic Cascade

Development of a Robust Numerical Optimization Methodology for Turbine Endwalls and Effect of Endwall Contouring on Turbine Passage Performance

Kapil Vitthalbhai Panchal

Abstract

Airfoil endwall contouring has been widely studied during the past two decades for the reduction of secondary losses in turbine passages. Although many endwall contouring methods have been suggested by researchers, an analytical tool based on the passage design parameters is still not available for designers. Hence, the best endwall contour shape is usually decided through an optimization study. Moreover, a general guideline for the endwall shape variation can be extrapolated from the existing literature. It has not been validated whether the optimum endwall shape for one passage can be fitted to other similar passage geometry to achieve, least of all a non-optimum but a definite, reduction in losses. Most published studies were conducted at low exit Mach numbers and only recently some studies on the effect of endwall contouring on aerodynamics performance of a turbine passage at high exit Mach numbers have been published. There is, however, no study available in the open literature for a very high turning blade with a transonic design exit Mach number and the effect of endwall contouring on the heat transfer performance of a turbine passage.

During the present study, a robust, aerodynamic performance based numerical optimization methodology for turbine endwall contouring has been developed. The methodology is also adaptable to a range of geometry optimization problems in turbomachinery. It is also possible to use the same methodology for multi-objective aero-thermal optimization. The methodology was applied to a high turning transonic turbine blade passage to achieve a geometry based on minimum total pressure loss criterion. The geometry was then compared with two other endwall geometries. The first geometry is based on minimum secondary kinetic energy value instead of minimum total pressure loss criterion. The second geometry is based on a curve combination based geometry generation method found in the literature. A normalized contoured surface topology was extracted from a previous study that has similar blade design parameters. This

surface was then fitted to the turbine passage under study in order to investigate the effect of such trend based surface fitting. Aerodynamic response of these geometries has been compared in detail with the baseline case without any endwall contouring.

A new non-contoured baseline design and two contoured endwall designs were provided by Siemens Energy, Inc. The pitch length for these designs is about 25% higher than the turbine passage used for the endwall optimization study. The aerodynamic performance of these endwalls was studied through numerical simulations. Heat transfer performance of these endwall geometries was experimentally investigated in the transonic turbine cascade facility at Virginia Tech. One of the contoured geometries was based on optimum aerodynamic loss reduction criterion while the other was based on optimum heat transfer performance criterion. All the three geometries were experimentally tested at design and off-design Mach number conditions. The study revealed that endwall contouring results in significant performance benefit from the heat transfer performance point of view.

Acknowledgements

I am indebted to Dr. Srinath Ekkad and Dr. Wing Ng, for their continuous support, encouragement and trust during the course of my doctoral studies. They both have been great sources of inspiration. I have learnt a lot, not only from their wealth of research expertise, but also from their practical, real-world point of view toward work. They have been a source of guidance for professional as well as personal development.

I am indebted to my parents and family for all the love. It was simply impossible to reach at this stage without their support.

I would like to express my sincere thanks to my advisory committee members Dr. Danesh Tafti, Dr. Clinton Dancey, and Dr. Mark Stremler for all the valuable suggestions and advice.

My special thanks also go to Santosh Abraham for helping me conduct all the heat transfer experiments. It has been a pleasure working with him during past three and a half years. I would like to thank Siemens Energy, Inc. for all the funding support during my studies and special thanks to Anthony Malandra and Andrew Lohaus from Siemens and Barry Brown from Florida Turbine Technology for all the valuable technical discussions and suggestions. I am also grateful to Song Xue, Colin Reagle and all the colleagues of research group for their help and support. Jaideep Pandit and Sridharan Ramesh have always been helpful and patient whenever I have been consuming all the available computational resources. Thank you so much. I would also like to thank staff members of Mechanical Engineering Department who have always been ready to help.

I would like to thank my friend Keyur Joshi, his wife Karuna Joshi and my roommate Kedar Vilankar. It has been a pleasure living with you all during the past two years. Shweta, you have always been a source of encouragement and support. There are many people from whom I have learnt many good things in life and that list is simply too long. My sincere thanks to all.

Last but not the least; I would like to thank huckleberry trail for providing a quiet and peaceful environment during all the weekend long walks that gave me time for thinking and reflection.

Table of Contents

List of Figures

List of Tables

Nomenclature

AO	Aero-optimized
C_{ax}	Axial chord length
h,HTC	Heat transfer coefficient
HTO	Heat transfer optimized
IP	Increased pitch
k	Thermal conductivity
M	Camera matrix, Mach number
M_{iso}	Isentropic Mach number $M_{iso} = \sqrt{\left(\frac{p_{0in}}{p_s}\right)^{\frac{\gamma-1}{\gamma}} - 1}$
p_{0in}	Pitchwise average stagnation pressure at inlet midspan
p_0	Local stagnation pressure
p_s	Local static pressure
p_{sexit}	Pitchwise average static pressure on angled endwall $0.5\,C_{ax}$ downstream of the trailing edge
PS	Pressure surface
q''	Heat flux
SKE	Secondary kinetic energy $\frac{\rho\left(v_{sec}^2+w_{sec}^2\right)}{2}$
SP	Short pitch
SS	Suction surface

t	Time
T	Temperature, T_∞ - mainstream temperature, T_w – wall temperature, T_i - initial temperature
v_{sec}	Secondary velocity in y direction
x, y, z	Cartesian co-ordinates
w	Uncertainty in measurements
w_{sec}	Secondary velocity in z direction

Greek Letters

α	Thermal diffusivity
ω	Loss coefficient $\frac{p_{0in}-p_0}{p_{0in}-p_{sexit}}$

Part A:

Development of a robust numerical optimization methodology and its application to a transonic turbine blade passage.

1. Introduction

1.1 Turbine aerodynamics and secondary flows

Despite many attempts made by researchers since the first secondary flow modeling attempt of Hawthorne [1] in 1955, as Langston [2] says in his historical review paper in 2001, the accurate routine prediction of secondary flow losses has not yet been achieved. Although the underlying detailed flow physics is still not understood very well, the main secondary flow structures common to any turbine passages have been identified and well documented. Every turbine designer wishes the flow to move in a so called primary or streamwise flow direction defined by the blade profile shape. However, the real flow effects, like the horseshoe vortex formation and passage vortex formation due to viscous effects at the endwalls, give rise to cross flow, called secondary flow or endwall flow, in a plane perpendicular to the primary flow direction. The term 'endwall' here refers to the side walls of linear cascade passage and hub or shroud walls of annular cascade or actual turbine passage.

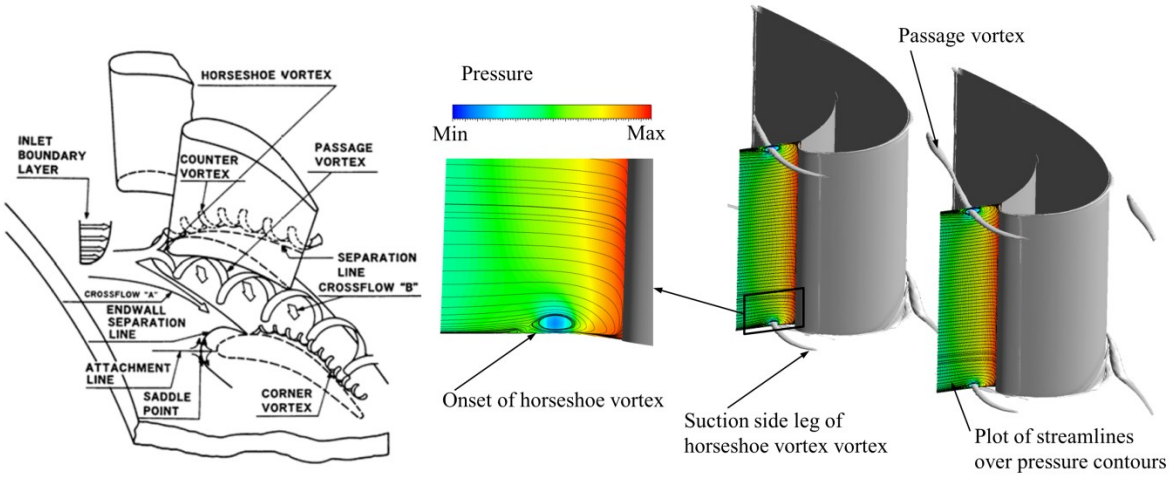

Figure 1 : (a) Secondary flow in turbine cascades (Takeishi [3]) (left) (b) Onset of horseshoe vortex near leading edge (right)

When the inlet flow approaches the blade leading edge, it either needs to decelerate to the stagnation point or change its direction either along the suction surface or the pressure surface. The difference of velocities in the incoming boundary layer results in different rate of deceleration and hence a rotational flow occurs near the leading edge–endwall junction. Hence, the inlet boundary layer flow rolls up into two legs of the horseshoe vortex (see Figure 1 (b))

near the junction of blade leading edge and endwall at a point called the saddle point. The vortex leg that follows the suction surface near endwall is called the suction leg and it transforms into the corner vortex along the suction surface as shown in Figure 1(a) [3]. The pressure side leg of the horseshoe vortex moves gradually in the cross passage direction and finally meets the passage vortex. The passage vortex is the vortex generated due to the cross passage flow of low momentum fluid from pressure side toward the high momentum fluid on the suction side near the endwalls. Many other additional secondary flow patterns have been suggested by many researchers such as that by Sharma and Butler [4] and Wang et al [5]. The aerodynamic losses attributed to the secondary flows can be as high as 30-50% of the total blade row loss according to Sharma and Butler [4]. Although many secondary flow patterns have been identified with relatively good understanding, the underlying loss generation mechanisms are not understood well yet. As Langston [2] said, "… must await either a better turbulence model or more experiments to reveal new endwall loss production mechanisms." Until then, turbine designers will have to rely on current methods involving use of empirical correlations, optimization methods and sometimes trial-and-error methods for passage flow control and loss reduction.

1.2 Methods of passage flow control and loss reduction

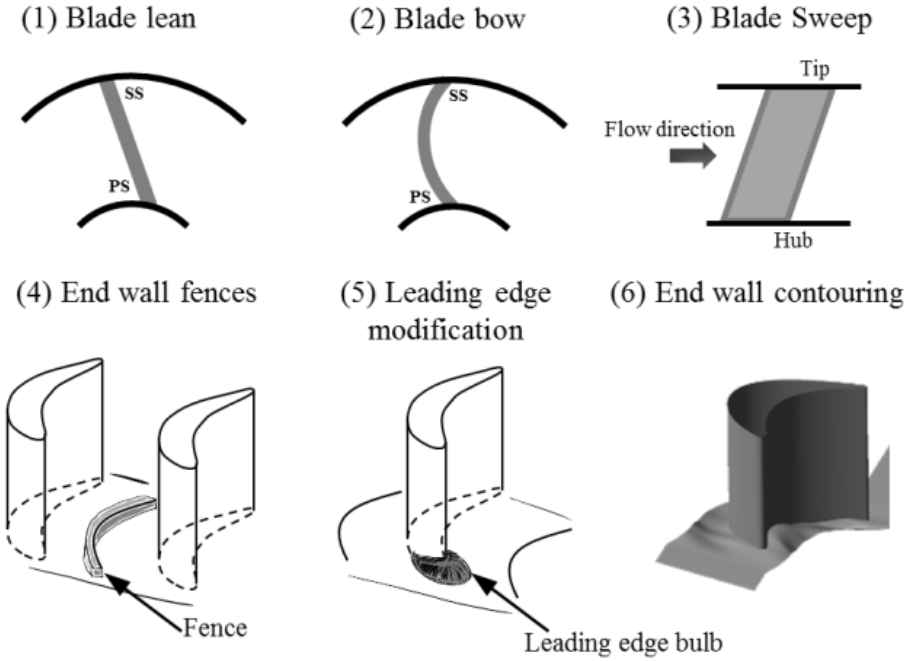

Figure 2 : Methods of passage flow control

Once the blade profile is available, the passage design methods for loss reduction can be primarily classified, as shown in Figure 2 into six groups as, (1) Blade lean, (2) Blade bow, (3) Blade sweep, (4) Endwall fences, (5) Leading edge modification and (6) Endwall contouring.

Although blade lean, bow and sweep are commonly used in gas turbine industry, they do not offer any significant loss reductions (Ref. [6]). Some blade sweep studies based on conventional design guidelines, for example [7], have even shown increased loss production. Endwall fences have shown reduction in secondary losses by modification of passage vortex direction (See [8; 9; 10]). Aunapu et al [10] observed that the effectiveness of endwall fences in reducing secondary losses decreases at low turbulence levels. Moreover, endwall fences can be create using grooves or obstructions at any place within the turbine passage. A definitive guideline for placement and shape of such fences is not available yet.

Leading edge modification can be considered as a type of endwall contouring in which only the endwall surface close to the leading edge is modified. Sauer et al [11] tested one such geometry in a low pressure turbine cascade with an aspect ratio of 3.0 at a Reynolds number of 4×10^5 and observed reduction of 47% in net secondary loss. Effect of such leading edge modification at high Reynolds number and Mach numbers is not known yet.

Much effort has been placed on the use of endwall contouring for the loss reduction in past two decades. Many researchers have achieved significant loss reduction, especially for low exit Mach number studies, through endwall contouring and some have observed redistribution of losses over the whole span. The following section presents endwall contouring methods in more details and describes the motivation for the present study.

2. Endwall contouring: Literature survey and motivation for study

2.1 Methods of endwall geometry generation

Many endwall contouring methods have been proposed in the past three decades of endwall contouring research. Fundamentally all the methods can be classified into either axisymmetric endwall contouring or non-axisymmetric endwall contouring methods. Axisymmetric endwall contouring methods attempt endwall contouring by contouring the endwall only in meridional direction and keeping the same contour shape in circumferential direction (pitchwise direction for linear cascades).

Most studies involving axisymmetric endwall contouring focused on changing the inlet span through such contouring. Some of such meridional contours are shown in Figure 3 below. Many of such endwall contouring studies report significant reduction in losses, but the fact that the span itself has been changed as compared to the reference span dimensions render such approaches unusable for a turbine designer who usually wants to achieve loss reduction without such changes in overall duct dimensions.

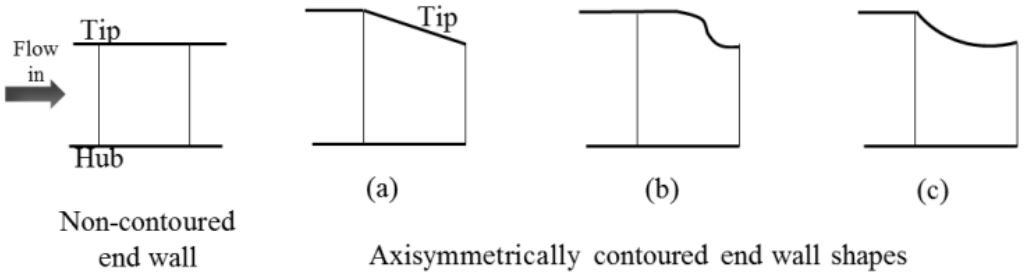

Figure 3 : Axisymmetric Endwall contour shapes

There are only two such studies, to the author's knowledge, where axisymmetric endwall contouring was applied without a change in overall duct dimensions. Atkins [12] studied the effect of axisymmetric endwall contouring on seven different profile geometries. However, no significant increase or decrease of loss was reported. Duden et al [13] studied the change in secondary loss due to three dimensional blade designs in a linear turbine cascade and later applied an axisymmetric endwall contour to this cascade. The study showed that most reduction

in losses occurred due to the 3D blade design. Axisymmetric endwall contouring resulted in insignificant increase in total loss.

As compared to the axisymmetric endwall design methods, many non-axisymmetric endwall contouring methods have shown promising improvements in loss characteristics. Non-axisymmetric contouring methods can usually be divided into three categories based on the method of specifying endwall surface topology. Such categories are: (a) Curve combination methods, where two curves are used to specify geometric variation in axial and pitchwise direction and then combination of these two curves can be represented as an analytic surface (See Figure 4 and Nagel et al [14], Saha and Acharya [15]); (b) Direct surface modification method, where the definition of a b-spline surface is modified directly by changing the location of surface control points (See Figure 4 and Praisner et al [16]) and (c) Hybrid method in which a surface is passed through a series of curves to generate endwall topology (See Figure 4 and Harvey et al [17]). There is yet no recommended method for endwall contouring. However, the designer should choose a method that is most flexible in terms of generating a wide range of surface topology.

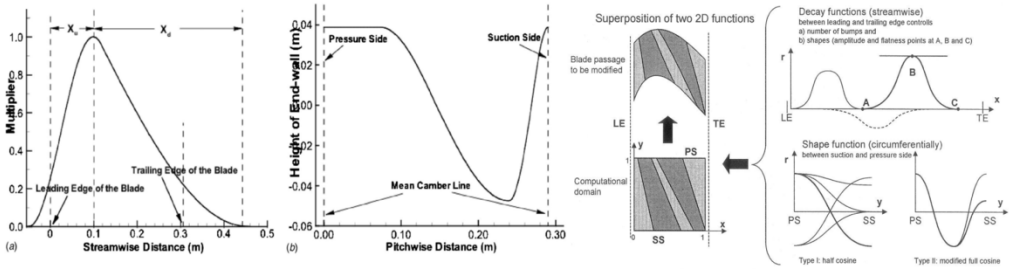

(A) Saha [15] (B) Nagel [14]

Curve combination based methods

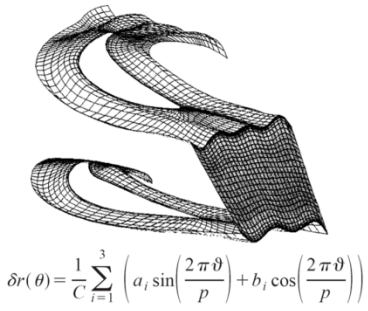

$$\delta r(\theta) = \frac{1}{C}\sum_{i=1}^{3}\left(a_i \sin\left(\frac{2\pi\vartheta}{p}\right) + b_i \cos\left(\frac{2\pi\vartheta}{p}\right)\right)$$

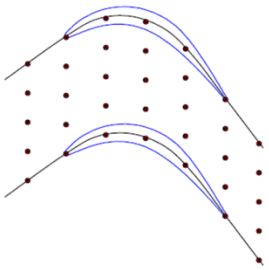

(C) Harvey [17] (D) Praisner [16]

Hybrid method Surface modification method

Figure 4 : Non-axisymmetric endwall contouring methods

2.2 Optimization objective for endwall contouring

Once a method for defining endwall surface is selected, the next step is to study the performance of a large number of geometries by changing the control parameters that define the shape of endwall surface. Two most widely used performance evaluation parameters are the stagnation pressure loss coefficient and the secondary kinetic energy (SKE) of the exit flow. A turbine designer, ideally, would want to have a passage design that results in theoretically maximum work transfer and near uniform flow distribution at the exit. However, in practice this is never achievable. The amount of work transfer is directly related to the reduction in total pressure loss and hence reduction of total pressure loss in the turbine passage is the main goal of a designer. A more uniform flow distribution at the exit can be achieved by reduction in mass average SKE and deviation angles at the passage exit plane. Deviation of flow direction from ideal exit direction results into increase in secondary kinetic energy and hence it is intuitively suggested that minimization of mass averaged SKE will also result in reduction in mass average deviation angles. Survey of available literature suggests that minimization of mass averaged total pressure loss usually results in reduction in SKE. However, comparison of the geometries obtained based on loss minimization and SKE minimization objective shows that the total pressure loss for the minimum SKE geometry is higher. Hence, total pressure loss is the preferred optimization criterion for endwall design.

Traditionally, mid-span pitchwise line average loss is considered as profile loss. Secondary loss values are calculated based on difference between mass averaged total loss and profile loss. However, such a calculation does not predict an accurate value of secondary losses because the underlying assumption that the profile losses are constant over the whole span is not true. Also, endwall contouring may affect the value of mid-span profile loss. Hence, total pressure loss based optimization should be based on the mass averaged value of loss coefficient and not the secondary loss coefficient.

2.3 Effects of endwall contouring and motivation for the present study

This section presents a review of important endwall contouring studies found in the literature. It is shown that most of the studies are very low exit Mach number investigations. Effect of

endwall contouring on high turning, transonic HP turbine blade passage is still an unchartered area.

During one of the earliest studies, Morris et al [18] studied the effect of meridional endwall contouring and demonstrated a reduction in overall secondary loss by 25%. The non-axisymmetric endwall profile used in the study, however, did not show any promising results. The study was conducted at a very low Mach number and Reynolds number as compared to those encountered in modern HP turbines.

Kopper et al [19] studied an axisymmetrically contoured vane passage at high exit Mach number of 0.85 and noted about 17% reduction in mass averaged total losses. The vane was a low turning angle (70^o) profile with a low aspect ratio of about 0.5. Mass contained in the secondary flow structures is a significant portion of the total mass flow in such cases. The secondary losses were over half of the total losses. The experiments conducted by Duden et al [12] with a different type of meridional endwall profiling, for a highly loaded turbine cascade with about 100^o turning, however, did not show any significant overall reduction in overall losses.

Many other researchers tried such axisymmetric endwall contouring (EWC), especially during the 1990s, but none of the studies showed significant and definite improvement for high exit Mach number blades.

Rose [20] proposed a method of nonaxisymmetric endwall contouring using a combination of two profiles in which these profiles specified axial and circumferential shape variations for the endwall of an HP turbine NGV. He suggested a sinusoidal circumferential profile variation for subsonic flow field and a Fourier series based profile variation for supersonic flow field.

Harvey et al [17] and Hartland et al [21] used a combination of Fourier series perturbations in the pitchwise direction and a b-spline curve fitted in the axial direction in order to generate nonaxisymmetric endwall profile for a 100^o turning turbine blade cascade. Experimental analysis carried out at a very low Mach number (~0.1) showed reduction in total loss by about 20%. CFD predictions used for the design iterations had reported a total loss reduction of only about 0.5%. This method has been used in many other cascade studies as well as real engine experiments and has been found to produce improved results for similar low exit Mach number applications.

Hartland [22] reported 6% reduction in secondary losses for and endwall surface that was defined using a half cosine wave in pitchwise direction and an axial profile based on the blade camber line shape.

Nagel et al [22] used combination of pressure and suction side shape functions with a circumferentially varying decay function to generate endwall profile for a turbine vane cascade. These functions were based on the passage design parameters. The exit Mach number for the flow was reported to be 0.59.

Saha et al [15] followed the approach of generating a geometry using a combination of streamwise and pitchwise height variation curves. They numerically studied nine geometries with such nonaxisymmetric contours. Reported reduction in mass averaged total losses was about 3.2% through numerical computations for the finally selected geometry. During the low Mach number experimental investigations for this blade profile, Gustafson et al [24] reported a 50% reduction in mass averaged pressure losses.

Prainser et al [16] used direct surface modification using control point heights to generate profiled endwall. Numerical computations showed 12% reduction in total row-loss for the optimized endwall. However, the experimental results showed 25% reduction for the same geometry. The exit Mach number was about 0.1, a very low value.

Few important observations can be made from this information. Firstly, most of these studies were done at low exit Mach numbers and for moderate turning airfoils. The only study that was performed at very high Mach number was done on an axisymmetrically profiled endwall of a vane. There has been no published computational or experimental study done on a high turning transonic blade at a high exit Mach numbers.

For the studies where numerical computations were used, CFD results often under predicted the magnitude of loss as well as the change in loss as compared to the experimental results. However, CFD results indeed captured the correct trends and the optimized geometries indeed showed improved performance.

A large variety of endwall contouring methods exists in literature. However, they broadly fall into either curve combination based method or direct surface modification method. These studies

indicate that it is possible to have a general guideline regarding the endwall shape variation along the flow passage. For example, Snedden et al [25] applied Durham cascade (ref. [17; 21]) hub profile to the annular endwall of a 1½ stage rotating rig and observed about 0.4% improvement in rotor efficiency. However, the rotor exit relative velocities were very low in the range of about 50 m/s. The sensitivity of change in loss values by fitting endwall contours designed for a high exit Mach number turbine passage to another turbine passage with similar design parameters has, however, not been studied.

Recently, Taremi et al [26] experimentally studied the effect of endwall contouring on a transonic cascade of HP turbine blades with a turning angle of about 112°. The study revealed that the loss reduction at $1.4\ C_{ax}$ location was negligible whereas that at $2.0\ C_{ax}$ location was found to be a comparatively small value of 7%.

The present study numerically investigates the effect of endwall contouring methods on a transonic blade passage. The blade profile used for the study represents a high turning (~127^{o}), high exit Mach number (M_{iso}~0.85) profile of the first stage of an HP turbine blade. The blade passage exit aspect ratio is 1.45.

The immediately following chapter describes the details of passage geometry generation, endwall geometry generation and corresponding mesh generation methods. Details of mesh refinement study, blade loading validation and mesh noise assessment have also been provided in the relevant chapter.

The present study provides details of the optimization methodology used for the endwall contouring of the transonic turbine blade profile. Two geometries, one with minimum total loss values and one with minimum SKE values, have been compared for their aerodynamic performance. In addition to that, the contouring method used by Saha et al [15] and Gustafson et al [24] has been normalized, scaled and applied to the passage under study. Both, the optimized and surface fitted endwalls were compared, in order to decide whether it is possible to achieve, even a non-optimum but certain, loss reduction by fitting an endwall contour shape of one blade passage to another blade passage with similar design parameters.

3. Endwall optimization methodology

The detailed optimization methodology for the endwall surface modification and optimization is presented in this chapter. The methodology uses routines, developed in house; to avoid the inherent problems associated with the surface modeling based geometry and mesh generation programs in most commercial mesh generators and hence is very robust. With due modification, this methodology can be adapted to a wide variety of turbomachinery geometry optimization cases. It is also possible to easily change the optimization objective and hence a heat transfer based optimization of the turbomachinery components is also possible. However, only aerodynamic performance based optimization has been described here.

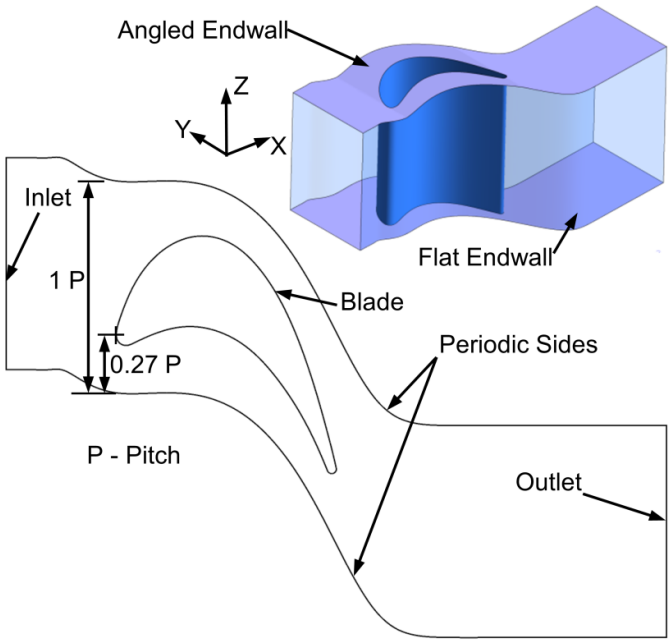

Figure 5 : 2D Passage Geometry

3.1 Passage geometry generation

A Matlab^{TM} routine, developed in-house, was used to generate the required passage curves for 3D CFD analysis. Initially the curves for the 2D turbine passage (Figure 5) are generated, which are then used to generate a 3D passage. The parameters for the b-spline curves for the periodic sides of the passage (Figure 5) can be selected and manipulated using the Matlab^{TM} routine. In order to closely simulate the blade loading which is similar to that on the actual blade,

the exit span is increased relative to the inlet span. This results in one endwall diverging from inlet to exit at an angle of 13^{o}. Hence, the passage represents a quasi 2D linear cascade. The inlet to the turbine passage model is 0.5 axial chords upstream of the axial leading edge and the outlet is located 1.5 axial chords downstream of the trailing edge.

3.2 Endwall geometry generation

Two different types of endwall geometries have been studied. However, the overall procedure for endwall surface generation for the simulation remains the same. A Matlab™ routine has been developed in-house that facilitates interactive placement of control points within the passage as shown in Figure 6. It is possible to place a set of control points at any axial location. Also, at a given axial location, any number of control points can be placed which are then used to generate a b-spline curve in pitchwise direction. The contoured surface passes through these control points. The axial direction represents the direction of engine axis.

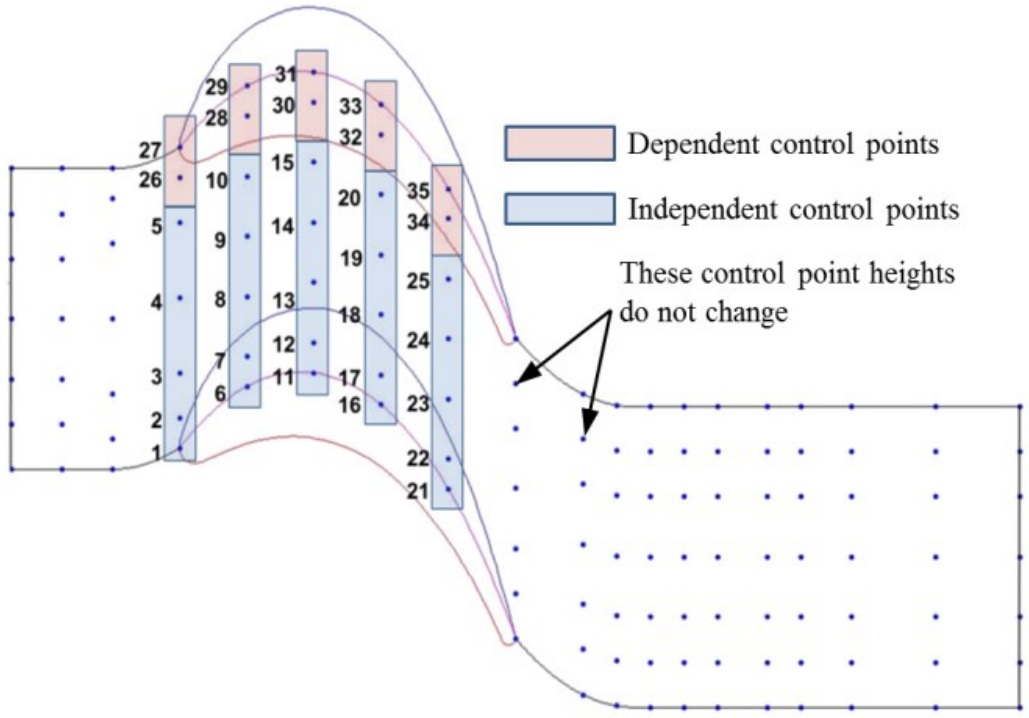

Figure 6 : Contoured Surface Control Point Placement

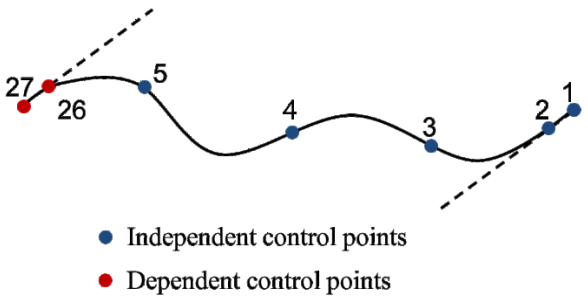

Figure 7 : B-Spline Curve Fitting At an Axial Location

At a given axial location, the set of control points has a certain number of independent control points as shown in Figure 6. Height, in the direction perpendicular to the page, of these control points can be changed independently. The heights of dependent control points are calculated in such a way that surface continuity is maintained in pitchwise direction. An example of such height adjustment is as shown in Figure 7 for a set of control points.

A set of parameter values for each independently controllable point, as a fraction of maximum height variation, is specified during design iterations. The maximum height variation, i.e. maximum peak or trough height in comparison to the non-contoured endwall, for this study was specified to be about $\pm 5\%$ of inlet span. The Matlab^{TM} routine decides the control point heights based on these parameter values. A b-spline curve is fitted to pass through these control points. The algorithm to fit such a b-spline was adopted from Ref. [27]. The heights of dependent control points are calculated in such a way that the b-spline maintains C^0 continuity and an approximate C^1 continuity in pitchwise direction. Heights of curve end points are restricted to be the same, for example points 1 and 27 in Figure 7, to maintain C^0 continuity. Second point from each end of the curve is used to maintain an approximate C^1 continuity. For example, height of the dependent control point 26 is set in such a way that the slop of line passing through points 27 and 26 is numerically close to the slope of line passing through points 1 and 2 as shown in Figure 7. Once the equation of b-spline at a given axial location is available, such a b-spline is extended multiple times in pitchwise direction on both the sides to ensure surface continuity during surface generation process. It may be noted that such continuity is required only in upstream and downstream regions. The control points span from one camber line to another camber line within the passage, as shown in Figure 6, and therefore, such continuity is not a requirement within the passage.

Once the curve points are available at each axial location, a surface is lofted through all the curves, which is the required contoured surface for specified parameter values. It is possible to have a very high flexibility in surface generation as any number of points can be specified at a given axial location. However, increased number of independent control point increases number of iterations required for the optimization process.

During the present study 25 control points within the passage were used as independent control points. This limits the extent of contouring from 1.25 axial chords upstream up to the axial trailing edge of the blade.

3.3 Passage mesh generation

A 2D mesh, as shown in Figure 8, is initially generated using ICEM CFD commercial mesh generation software.

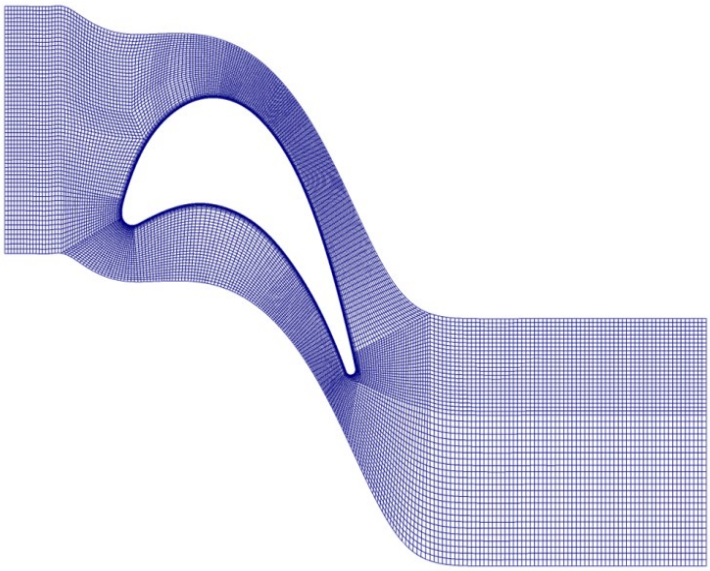

Figure 8 : Initial 2D Mesh and corresponding block structure

This mesh is then used as input to a Matlab^{TM} routine that generates 3D baseline mesh with non-contoured angled endwall as shown in Figure 9. The mesh generated by the routine is a very high quality mesh with minimum mesh quality of 0.5 and a highly orthogonal mesh with about 92% of cells with minimum angle of 63^{o}. Minimum angle for the whole domain was found to be

27^{o}. The final mesh used after mesh refinement study showed y^{+} values below or close to 1 for most of the region with the highest y^{+} values close to 2 in a small region near trailing edge.

3.4 Mesh modification for endwall contours

Most commercially available grid generation software programs have surface modeling based geometry generation. This creates problems related to surface stitching where two surfaces meet at an angle, especially when mesh generation is automated. In addition, negative volume problems are generally encountered when mesh needs to be projected on to a highly distorted contoured surfaces like those used in the present study.

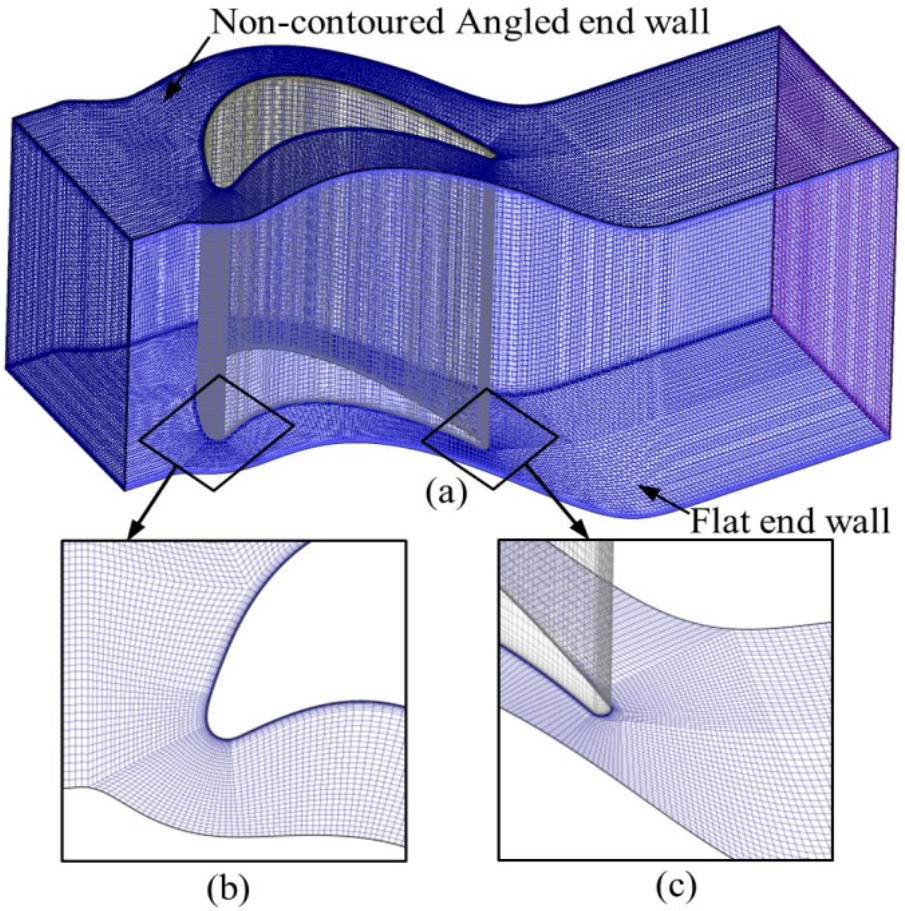

Figure 9 : (A) 3D Baseline Mesh with One Angled Endwall (B) Enlarged region near leading edge (C) Enlarged region near trailing edge

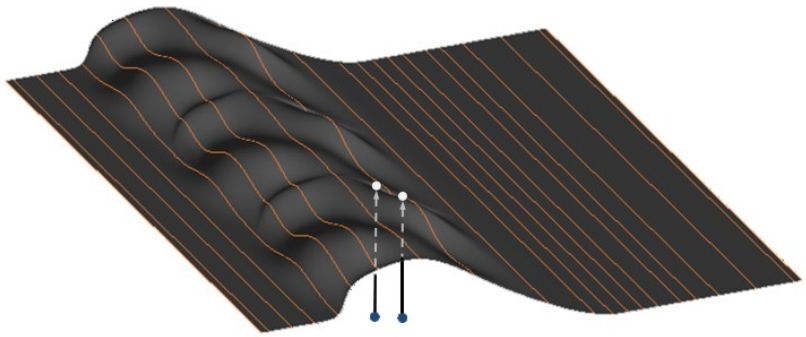

Figure 10 : Node Projection Based Mesh Modification

A Matlab^{TM} routine was developed, that avoids mesh generation problems. The b-spline curves are used to generate a lofted contoured surface as mentioned before. An example of the pitchwise extended contoured endwall surface is shown in Figure 10.

It may be noted that the contouring was done on the angled endwall. The distance between mesh nodes on flat endwall and corresponding mesh nodes on the contoured endwall is calculated by projecting the non-contoured angled endwall nodes on the contoured endwall. All the mesh points are then shifted in spanwise direction using the MATLAB^{TM} routine in order to accommodate the change in heights at different locations. It was observed that the mesh used for this study is sufficiently dense and hence there was not much mesh distortion due to such node movement.

Such a node projection based approach facilitates very robust automated mesh generation capability which is essential for optimization runs. The routine is able to successfully generate good mesh even for highly contoured geometries.

3.5 Endwall contouring optimization

A commercial optimization package, Isight 4.0, was used for this optimization study. Gradient based methods are usually more robust as compared to the random search algorithms like genetic algorithms. Hence, sequential quadratic programming (SQP) gradient based optimization technique was used. The optimization loop is shown in Figure 11. The gradient step size used was 0.05 as mentioned in the mesh noise assessment study. The optimization objective was to minimize total loss coefficient 1.0 axial chord downstream of the trailing edge. Range of

variation for each parameter was specified as a constraint condition. Additionally, a constraint was specified to restrict the maximum variation in passage mass flow rate by ±1% of the baseline geometry mass flow rate. An optimized geometry was achieved after about 350 contour geometry evaluations. The mesh generation program worked reliably. No failed runs were encountered during optimization process. Characteristics of optimized geometry are discussed in the "Results and discussion" section, where this optimized geometry is referred to as "Geometry A".

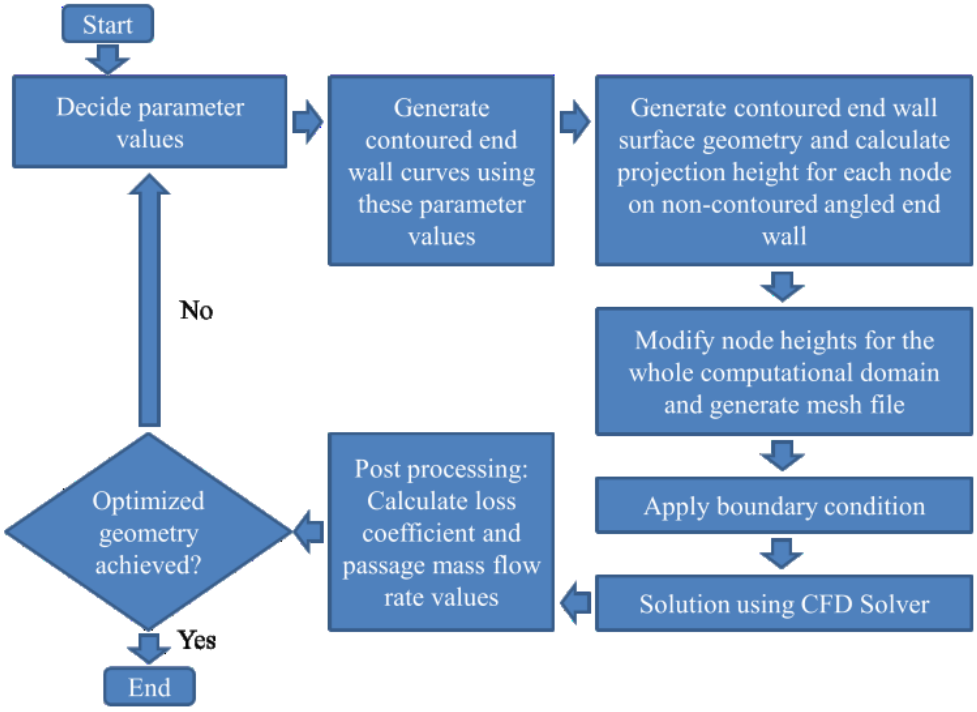

Figure 11 : Optimization Algorithm

Once the optimization was complete, another optimization loop with genetic algorithm based optimization was run to ensure that the optimum geometry achieved by the SQP method is a globally optimum geometry and not a locally optimum one. The limit of population was set to 500 iterations. The program was stopped after 500 iterations and hence could not achieve a final optimum. However, the optimum geometry available from the 500 iterations showed a clear trend of peaks and troughs of the contours that resemble those found in the SQP based optimum geometry. Hence, it can be safely assumed that the SQP based optimum geometry is the globally optimum geometry.

4. Application of endwall contouring optimization methodology to a transonic turbine blade endwall

4.1 CFD model and boundary conditions

Various boundary conditions applied on the model are shown in Fig. 1. Inlet total pressure profile was experimentally measured and applied as inlet boundary condition. Uniform total temperature conditions were specified at the inlet. Due to the very high turning angle of the blades, the flow starts turning even before the leading edge and an induced incidence angle is observed just before the leading edge. Hence, a slightly positive incidence angle was specified at the inlet in order to get design incidence angle near the blade leading edge. Once the simulation results were available, many contoured geometries were checked to confirm that the flow close to the blade leading edge closely matches the design inlet angle. This ensures correct design angle during the optimization study. Medium turbulence intensity of 5%, that closely matches the turbulence level observed during the experimental study done on this blade passage, was specified at the inlet boundary.

Prescribed average static pressure condition was specified at the outlet boundaries. Translational periodic boundary conditions were prescribed at the periodic sides. Endwalls and blade surface were prescribed adiabatic wall boundary condition with zero slip velocity.

SST $k-\omega$ turbulence model was used based on past experience. Convergence criteria form RMS residuals was chosen to be 5×10^{-5} based on the mesh refinement study. The CFD solver produced airfoil loading results, that are in reasonably good agreement with the experimental results as shown in Fig. 7 and hence the code is considered validated.

Fully 3D, viscous CFD solver CFX version 12.1 was used for the simulations performed in this study.

4.2 Mesh refinement study and validation

Three grids with a uniform mesh refinement factor of 1.5 were used for the mesh refinement study on the baseline (non-contoured) geometry. The number of nodes in baseline mesh is about 1.5^3 times more than coarse mesh as the refinement is uniform in each direction. Similarly, the

number of nodes in fine mesh is about 1.5^3 times more than those in baseline mesh as shown in Table 1. The mesh uses near wall grid bunching close to the blade and the endwalls to simulate boundary layer flow more accurately. This bunching was selected in such a way that y^+ values remain below 1 for fine and baseline mesh and close to 1 for coarse mesh for most of the domain cells.

The objective of the optimization study was to minimize the total pressure loss 1.0 axial chord downstream of the axial trailing edge. Hence, this loss coefficient was chosen as the performance parameter for the refinement study. CFD simulations were performed for all the meshes with identical boundary conditions. Richardson extrapolation method was used to calculate the observed order of accuracy of the scheme. Simulation results were obtained with very stringent convergence criteria for RMS residuals, e.g. 1×10^{-12} for the baseline mesh, and were used in the Richardson extrapolation formula as the exact solution of discretized equations. The observed order of accuracy for the CFD scheme used was found to be 1.37. The magnitude of discretization error in the value of the loss coefficient at design condition, found based on the Richardson extrapolation method, was about 6.5% of the loss coefficient value, based on this observed order of accuracy [28]. Although the basic scheme is second order accurate, the overall formal order of accuracy of the CFD solver used is not known. Hence, it was not possible to calculate Roche's grid convergence index. However, for most commercial second order schemes, the formal order of accuracy is estimated to be well below second order and therefore the discretization error estimate of 6.5% is considered sufficiently accurate.

Table 1 : Mesh Sizes Used For Refinement Study

Mesh	Number of nodes
Coarse	591468
Baseline	1812030
Fine	6559938

The blade loading for the baseline case without endwall contouring at design conditions was compared with the experimental results. The results agree reasonably well as shown in Figure 12. It was observed, however, that the wake mixing after the trailing edge is not as rapid in CFD as compared to that observed in the experiments. Additionally, it was observed that the CFD results under-predict the loss coefficient values. However, many researchers mentioned in the

introduction section have stated the same observation. It seems that the optimized endwalls, however, do show improved results during the experimental studies in terms of loss coefficient or secondary kinetic energy. Comparison of the experimental and numerical results [29] showed that the CFD results, indeed, predicated the correct trend of loss coefficient values as observed in experimental results at various Mach numbers and incidence angles. Hence, such CFD simulations are considered to predict correct qualitative trends.

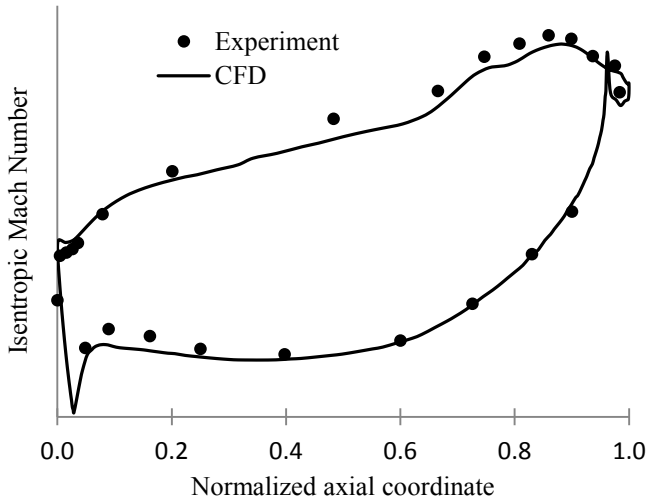

Figure 12 : Experimental and CFD Results For Blade Loading At Design Conditions

4.3 Mesh Noise Assessment

The optimization procedure mentioned in ensuing text evaluated hundreds of contour geometries. It was essential to confirm that, for the small change in parameter values, the mesh does not give noisy results due to mesh distortion. Also, this provides a reasonable value of the minimum step size for SQP based optimization method. This is established by taking a vector of all the parameters and varying the parameter values with a constant relative step size within the range of each such parameter. Some arbitrarily chosen parameters are varied from maximum to minimum values whereas the others are varied from minimum to maximum. The step size is decreased until the mesh no longer produces a smooth variation in performance parameter. This sets the limit of minimum step size for the gradient based optimization method used in this study.

The results of the noise assessment are as shown in Figure 13. It can be seen that the variation is smooth until step number 15. However, the contour geometries beyond step 15 were

found to be very aggressive and showed very high loss coefficient values. Hence, it can be considered that the mesh under study is sufficiently dense to give smooth monotonous variation of loss coefficient when the changes in parameter values are sufficiently small and the optimization objective is total loss minimization. The final step size chosen was 0.05 based on the results of noise assessment study.

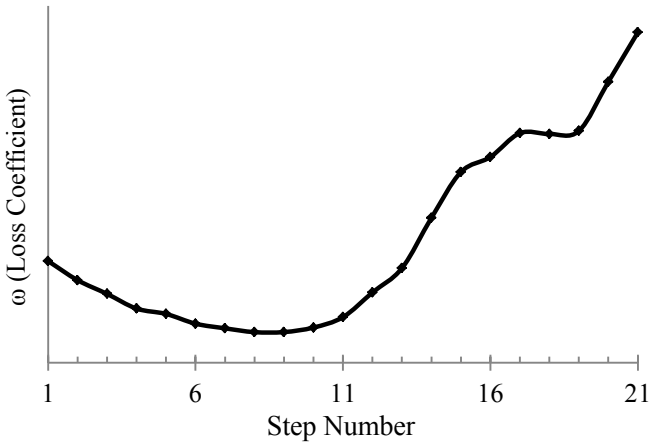

Figure 13 : Mesh Noise Assessment

4.4 Minimum SKE geometry

Out of all the geometries evaluated, it was found that the geometry that gives minimum total loss and the geometry that gives minimum secondary kinetic energy value 1.0 axial chord downstream of the trailing edge are different. Hence, the geometry that gives minimum SKE values (Geometry B) has also been considered in this study and compared with the loss optimized Geometry A.

4.5 Shape function based endwall geometry

It was mentioned in the "Introduction" section that Saha et al [15] numerically tested many pitchwise and streamwise curve combination based endwall geometries and Gustafson et al [24] experimentally tested the geometry giving the best performance. The design point values and geometric dimensions for the blade used in their study are to some extent similar to the blade used in this study. Hence, the curves used for the best geometry were digitized, normalized and scaled to fit the geometry under study. Once the geometry for this endwall contours was available, a mesh file was generated using the same procedure mentioned in the previous

sections. Comparison of this endwall geometry (called Geometry C) to the optimized geometry (Geometry A) is discussed in the ensuing section.

4.6 Results and discussion

Geometry A (total loss optimized geometry), geometry B (geometry with minimum SKE value) and the geometry C (based on a curve combination based method from literature) all showed negligible variation in passage mass flow rate and inlet flow angle as compared to the non-contoured baseline geometry.

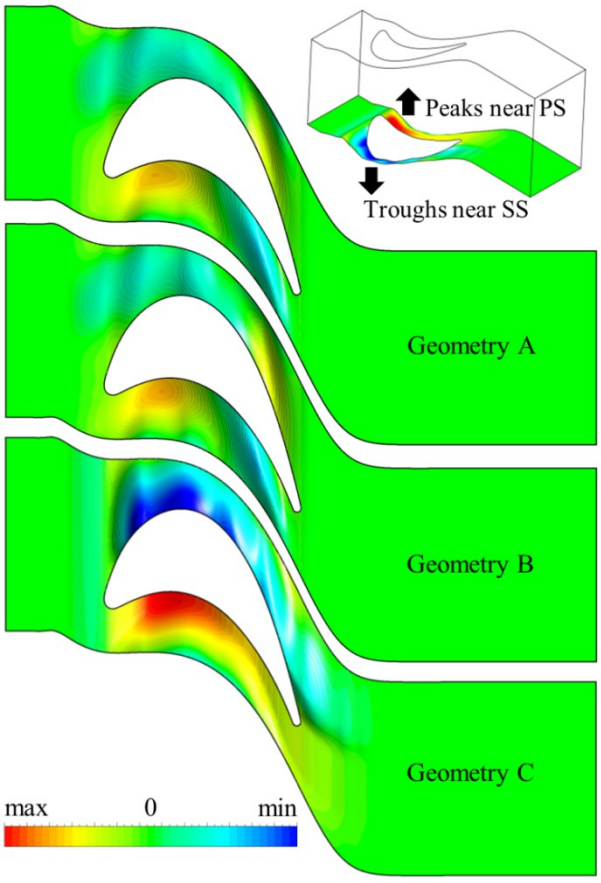

Figure 14 : Endwall Contour Heights for Geometries A, B and C

Endwall contours for all the three geometries are as shown in Figure 14. All the geometries show similar trend for peak and trough locations to that found in literature. There is a prominent high elevation region near pressure surface at about $0.2\,C_{ax}$ location within the passage and a trough near the suction surface at the same location. This type of contours could not have been possible for an axisymmetrically contoured endwall and hence the importance of a non-

axisymmetric contouring is evident. It may be noted that endwall contouring was restricted up to the axial trailing edge for geometries A and B. However, such restriction was not present for geometry C.

The peaks and troughs near trailing edge region are similarly prominent for all the geometries. However, such peaks occur near suction surface and troughs near pressure surface (opposite arrangement as compared to those at $0.2\ C_{ax}$ location) for geometry A and B, whereas such peaks appear near pressure surface for geometry C and the troughs near suction surface (similar arrangement as compared to those at $0.2\ C_{ax}$).

Figure 15 shows variation of mass averaged total pressure loss coefficient for all the geometries including the baseline case starting from leading edge up to $1.0\ C_{ax}$ downstream of the axial trailing edge. The values of loss coefficient are percentile fraction of the loss coefficient for the baseline case at a location $1.0\ C_{ax}$ downstream of the trailing edge. Geometries A and B do not show much change in loss coefficient whereas geometry C shows higher loss coefficient values throughout the passage length.

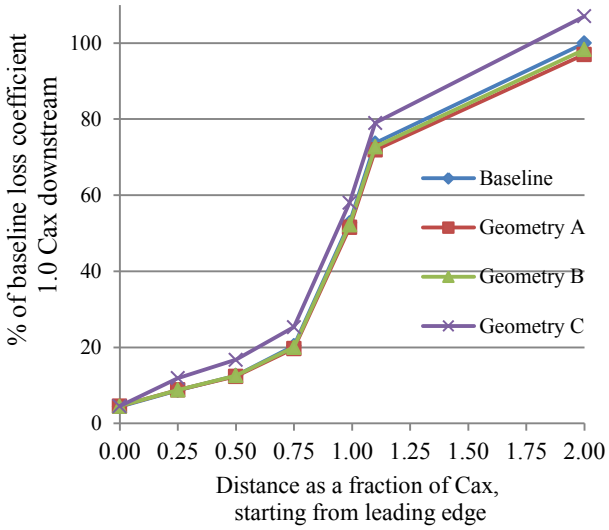

Figure 15 : Mass Averaged Total Pressure Loss Variation in Turbine Passage

It may be noted that there is marked increase in loss near trailing edge region within the passage. However, the slope of loss increase is almost the same for all the geometries. As mentioned, the prominent peak and trough locations are opposite for geometry C as compared to

geometry A and geometry B in trailing edge region but the increase of loss in this region is almost the same. This indicates that for this geometry the location of peaks and troughs in the trailing edge region do not help much in reducing the losses. This also suggests that because the passage vortex height from the endwall is the highest in the trailing edge region and hence the range of maximum variation in contour height should be wider in this region in order to effectively control the secondary flow. However, there will be a limit to such maximum height variation due to the constraints on possible throat area change. This also suggests that endwall contours in the frontal region of the passage, where passage vortex mixes with corner vortex, play a significant role in loss reduction.

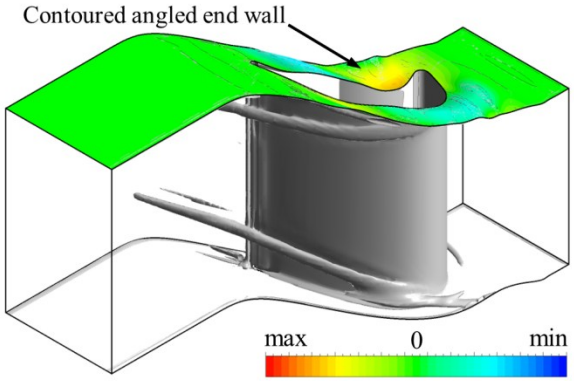

Figure 16 : Contour Heights and Flow Structure within Passage for Geometry A

Figure 16 shows that for the loss optimized geometry A the location of maximum trough near the leading edge region closely matches the location where the passage vortex mixes with the suction side horseshoe leg. Such a mixing location is to some extent controlled by the geometry contours. As this mixing location for the non-contoured geometry is different for different airfoil profile, this suggests that even though the general trend of higher elevation from pressure side to lower elevation of contours toward suction side is maintained, the actual location and heights of the peaks and trough significantly affects the amount of loss reduction. Although it may be possible to correlate heights of contours in the mixing region as a function of blade aspect ratio and over all Mach number range by studying a large number of contoured geometries, the location of the mixing region depends not only on the overall design parameters but also on the pressure loading variation on the blade surface. Hence, it is not certain whether it is possible to reasonably predict the location of this mixing region based on the overall blade design

parameters. This suggests that the optimized geometry for any blade profile should be obtained on case by case bases.

When compared for loss reduction performance, it was found that geometry A gives maximum reduction of about 3 % in comparison to geometry B (1.7%) in mass averaged total pressure loss at a location 1.0 C_{ax} downstream of the trailing edge. Geometry C showed an increase in loss coefficient by 7.0%. This again suggests that endwall contouring should be done on case by case bases and a general guideline may not always results in loss reduction. Table 2 shows loss performance of geometry A in comparison to the baseline geometry. The locations mentioned in the table are shown in Figure 17.

Plots of midspan blade loading for all the geometries were found to be almost on top of that for the baseline case and hence it was expected that the profile losses may not change due to contouring which is evident from the numerical values of profile loss in Table 2. It may be noted that all the numerical values in Table 2 are shown as percentage of loss coefficient for baseline case at location (3) shown in Figure 17.

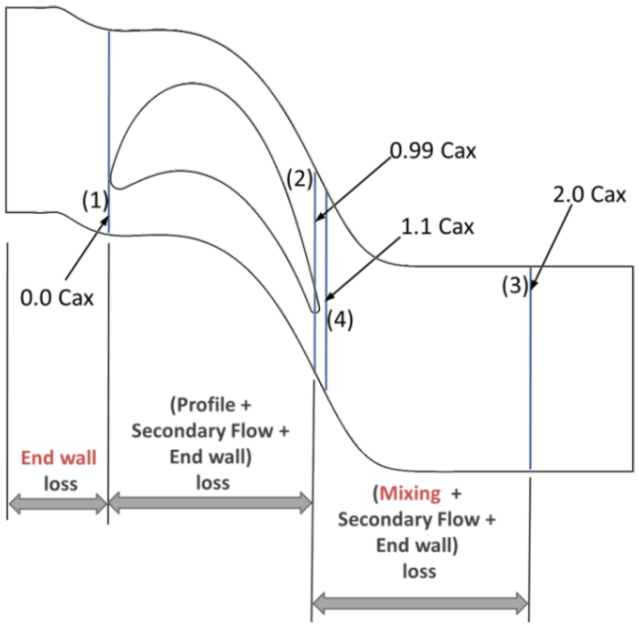

Figure 17 : Locations Of Loss Measurement

Table 2 : Loss Performance Of Geometry A In Comparison To The Baseline Geometry

Type of mass averaged total pressure loss and (location).	**% fraction of mass averaged total pressure loss for baseline geometry at location (3)**		
	Baseline (i)	**Geometry A (ii)**	**% Change [(ii) –(i)]/(i)**
Total loss (2)	53.24	51.81	- 2.68
Profile loss (2) (on a 5mm wide strip centered at mid-span)	38.55	38.12	-0.08
Endwall loss + secondary loss (2)	14.69	13.69	-6.81
Total loss (3)	**100.00**	97.0	-3.00
Mixing loss + endwall loss + secondary loss (3)	46.76	45.19	-3.35

Profile losses for such high turning high exit Mach number blades are as much as 50% of the total losses at location (3). The secondary and endwall loss within the passage is a small amount of about 2%. Also note that even if the reduction in secondary loss is about 6.81%, it is in fact a very small percentage of the total loss that occurs up to location (3). Readers should note that the secondary loss was calculated from profile and total loss calculations. Particularly, profile loss is calculated using mass averaged loss value on an area (on a 5mm wide strip) centered at mid-span. Such a calculation may give very high value of profile loss and may result in a considerably inaccurate value of secondary loss prediction. Therefore, for such blades, the optimization should be based on the total loss reduction objective instead of secondary loss minimization.

Comparison of mass averaged total loss suggests that endwall contouring results in a small percentage gain for such high turning blades subjected at high exit Mach numbers. For the baseline geometry the product of loss and mass flow in secondary flow region is about 25% of that for the whole area at location (2). Hence, an approximately 7% reduction in the secondary loss results into only a 1.75% reduction in mass averaged total pressure loss. The other reduction comes from reduction in profile loss.

It may be noted that the secondary flow, endwall and mixing losses that occur after the trailing edge account for as nearly as 47%. Endwall contouring for geometry A was restricted up to the axial trailing edge and still it helped in reduction of losses further downstream. In that case, it can be expected that endwall contouring in the downstream region may provide additional benefits.

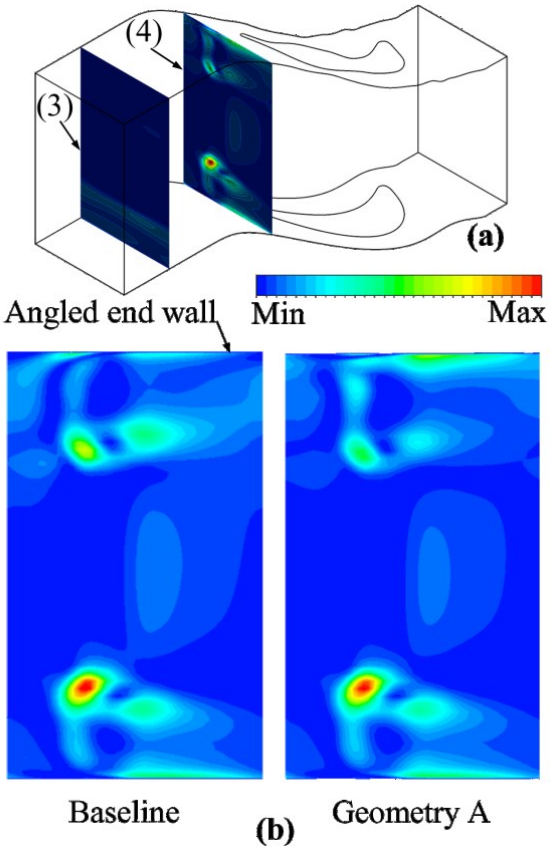

Figure 18 : Comparison of SKE Contours For Baseline and Geometry A At Location (4)

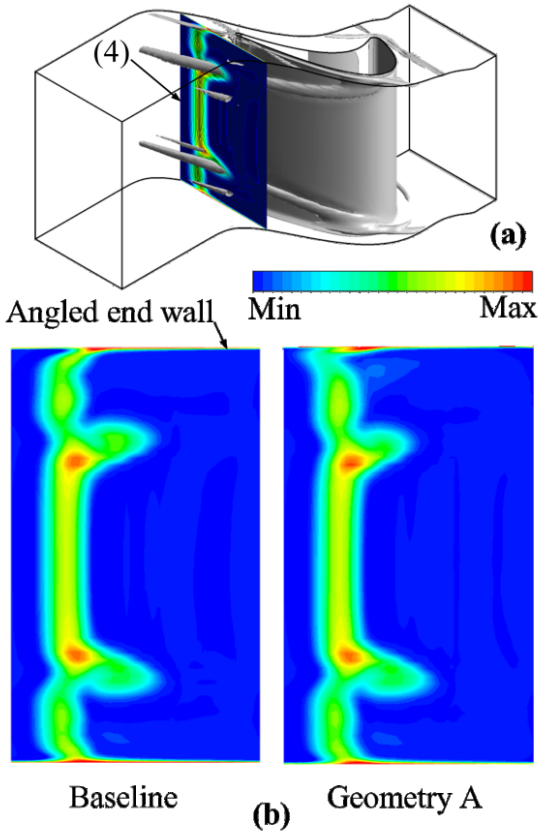

Figure 19 : Comparison of Loss Coefficient Contours For Baseline And Geometry A At Location (4)

It was found that losses and SKE are reasonably well mixed at location (3) as seen in Figure 18(a) hence the following discussion is limited to the losses and SKE at location (4) near trailing edge. The reduction in SKE values at location (3) for geometry with minimum SKE value (geometry B) was found to be about 24% as compared to the baseline case, whereas that for the Geometry A was found to be about 22%. As the difference in reduction is not much between geometry A and geometry B, only the losses and SKE for the baseline and the loss optimized geometry A have been presented here. Figure 18(b) shows SKE contours at location (4) for the

baseline geometry and geometry A. It can be seen that on the flat endwall side there is a region of very high secondary kinetic energy which is not seen on the angled endwall side. The reduction in SKE for geometry A as compared to baseline geometry is small and occurs close to the contoured endwall only. The endwall contouring for this case does not affect the flow on the opposite endwall. This is expected considering the high aspect ratio of the blade. There seems to be additional SKE production near the contoured endwall as compared to baseline due to endwall contour guided flow near trailing edge as evident from Figure 14 and Figure 16.

However, there is overall reduction of SKE at this location. The reduction in SKE can also be inferred from the reduced passage vortex strength as seen in Figure 20.

Similarly, the loss contours for both the geometries as shown in Figure 19(b) show that the reduction in losses seems to be only near the contoured endwall in passage vortex region with a slight increase in losses near the contoured endwall. This can also be seen from reduced strength of passage vortex in the trailing edge region on contoured endwall side in Figure 20.

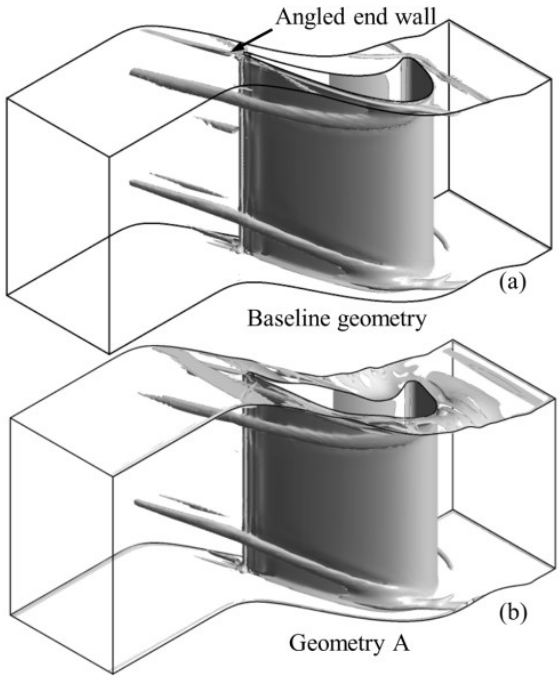

Figure 20 : Isosurface of Swirling Strength For Baseline And Geometry A

The region where highest loss occurs is the suction side corner vortex region as seen in Figure 19(a) and (b). Endwall contouring does not result into loss reduction in this region. Almost all of the reduction in loss seems to be due to reduction of losses in passage vortex

region. In may be noted that even if the loss values are very high in corner vortex region, velocities are low and hence the mass averaged loss coefficient is affected mainly by the reduction that takes place in the passage vortex region.

Comparison of SKE contours from Figure 18 and loss contours from Figure 19 suggests that for the baseline geometry, even if SKE values are low on the angled endwall side as compared to the flat endwall side, the loss coefficient values are almost symmetrically distributed near both the endwalls. Same observation can be made for geometry A. Hence, it can be concluded that SKE is not a primary factor that affects loss production. In that case, SKE values should not be included in endwall optimization unless better flow distribution is also an objective. In fact, the total pressure loss optimized geometry will generally provide a near optimum SKE reduction.

Part B:

Effect of Endwall Contouring on a Turbine Passage with Increased Pitch

5. Motivation

The results in the previous part of the study revealed that the endwall contouring for such high speed, high turning blades, provides a small benefit. This is due to the fact that the secondary losses are a small part of the total stagnation pressure losses. Therefore, even a significant amount of reduction in the secondary losses contributes to a small reduction in the overall losses for the turbine. However, endwall contouring may prove to be beneficial for a turbine passage, in which contribution of the secondary losses is higher.

This conclusion gave an opportunity to increase the blade pitch. Increasing the pitch and thereby reducing the blade count increases work transfer per blade. A higher blade loading results into higher secondary flow and thereby higher secondary losses. However, the reduced blade count may benefit in terms of lower engine weight and lower film cooling flow requirements. In such a case, if the increased pitch (IP) contour design can reduce the total pressure losses back to the level of original short pitch (SP) geometry, then the benefits of increasing the pitch can be realized. However, such a scheme would only work if the heat transfer performance of a contoured endwall either remains the same as the IP baseline endwall or improves.

Based on this philosophy, three endwall geometry designs were provided by Siemens Energy, Inc. The first geometry is the increased pitch non-contoured angled endwall with the same angle as that used for the short pitch baseline. The other two geometries are contoured endwall geometries where one was obtained with the aim to minimize aerodynamic loss and the other was obtained to minimize the net heat transfer through the endwall.

The aerodynamic performance of the endwalls was studied through numerical simulations. In the present study, the heat transfer performance of the endwalls was studied through experimental investigations. The effect of endwall contouring on heat transfer performance of the IP baseline and IP contoured endwalls was studied in detail.

6. Aerodynamic Performance

6.1 Comparison of IP and SP baselines

The pitch length was increased by 24.5% for the IP geometries as compared to the SP case. The consequent increase in the midspan blade loading for the IP baseline case can be seen in Figure 21 below. It was observed that the mid-span blade loading on the IP baseline increased by 33% due to such increase in pitch.

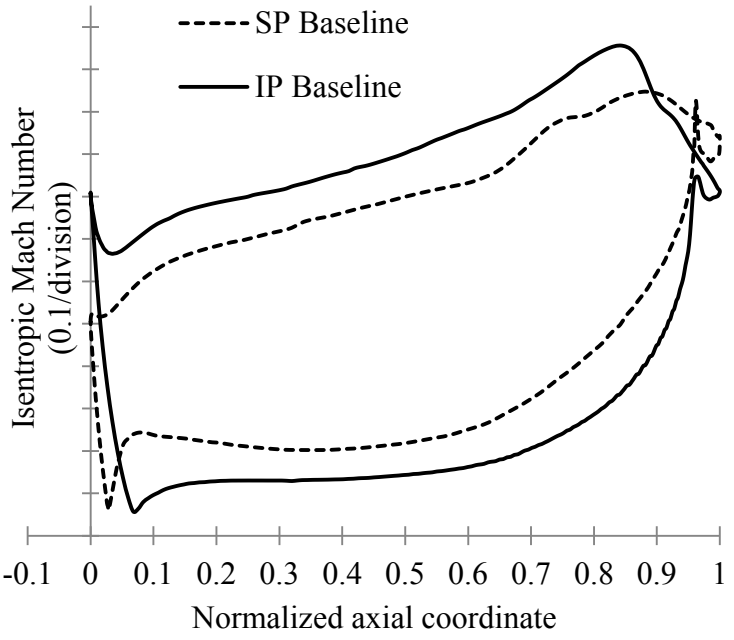

Figure 21 : Comparison of Mach number (Blade Loading) Distribution for SP and IP baseline designs

Such a higher blade loading creates higher pressure difference between the SS and PS sides of the passage and therefore results in a stronger cross flow from the PS toward the SS near the endwalls. The higher cross-flow adds to the passage vortex, which in turn results into higher secondary flow. Figure 22 on the next page shows secondary flow vortex cores for both the SP and IP designs. The vortex cores are plotted for the same values of swirling strength and therefore the bigger the vortex core for a given value of swirling strength, the stronger the secondary flow and consequent higher secondary losses.

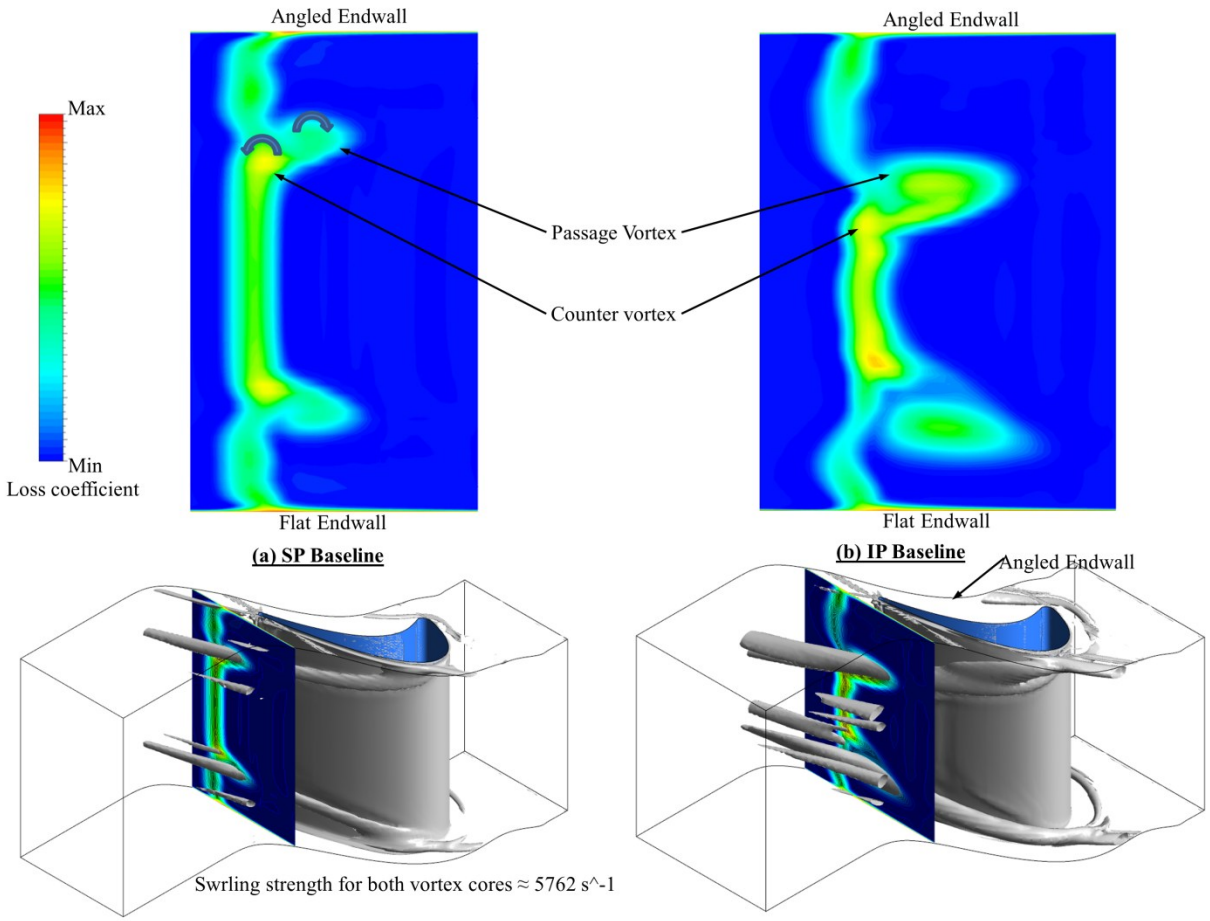

Figure 22: Comparison of SP and IP baseline secondary flow and losses

The mass contained in the secondary flow for the SP and IP baseline geometries, at $1.1\ C_{ax}$ location, was 7.2% and 14.7% respectively of the total mass flow rates for the corresponding geometries. Similarly, the secondary losses also showed elevated values. However, as mentioned in the previous part of the study, the product of loss and mass flow rate is the deciding factor about potential of benefit from endwall contouring. The product of loss coefficient and mass flow in the secondary flow region was found to be about 24% of the total value for the passage for the SP baseline, whereas that for the IP baseline was found to be about 52% of the total value for the passage, a clear increase of secondary losses by more than 100%. It was observed that the mass averaged total pressure loss at $2.0\ C_{ax}$ location increased by 8.6%. Therefore, it can be concluded that the IP baseline definitely shows more promise for potential benefit from the endwall contouring.

6.2 Comparison of IP endwall geometries.

In addition to the IP baseline design, two contoured geometries were provided by Siemens Energy, Inc. First contour geometry was designed based on the minimum aerodynamic loss criterion (AO geometry) whereas the second contour geometry was designed based on the minimum endwall heat transfer criterion (HTO geometry).

Figure 23 on the next page shows blade loading near the endwall for all the three geometries. Additionally, the secondary flow is shown using vortex cores. The change in local heights of the endwall in comparison to the baseline case for both the AO and HTO geometries is also shown. Figure 24 shows velocity contours and streamlines in near endwall region. It can be seen that the baseline endwall shows significant unloading of the blade in the near endwall region. The low momentum fluid being added from the pressure side toward the suction side increases pressure and thereby reduces Mach number in the region where the passage vortex meets the suction sidel leg of the horseshoe vortex. This meeting point and the path of movement of the passage vortex are also shown in the Figure 23. It can be seen that the AO endwall has large peak region near the pressure surface that extends up to the middle passage region in the aft section of the passage. There is also a valley region near the leading edge suction surface. Two more valleys in the aft region form a ridge in the middle aft section of the passage. This arrangement favors higher velocities in the leading edge suction side region and there by lowers the strength of the pressure side leg of the horseshoe vortex. The higher velocities on the suction side guide the passage vortex along the peak regions of the passage. This helps in avoiding the meeting point of the passage vortex and the suction side leg of the horseshoe vortex for a longer distance along the passage thereby avoiding the total pressure losses related to mixing. It can be observed that this kind of endwall also tends to distribute the blade loading more uniformly along the passage as compared to the baseline.

The heat transfer optimized endwall, however, extends the meeting point of the passage vortex and the SS side of horseshoe vortex only up to a small length and does not help in reducing the strength of the passage vortex significantly. Additionally, due to the high peak region in the aft section near suction side, the blade loading distribution shows a very non-uniform pattern as similar to the baseline case.

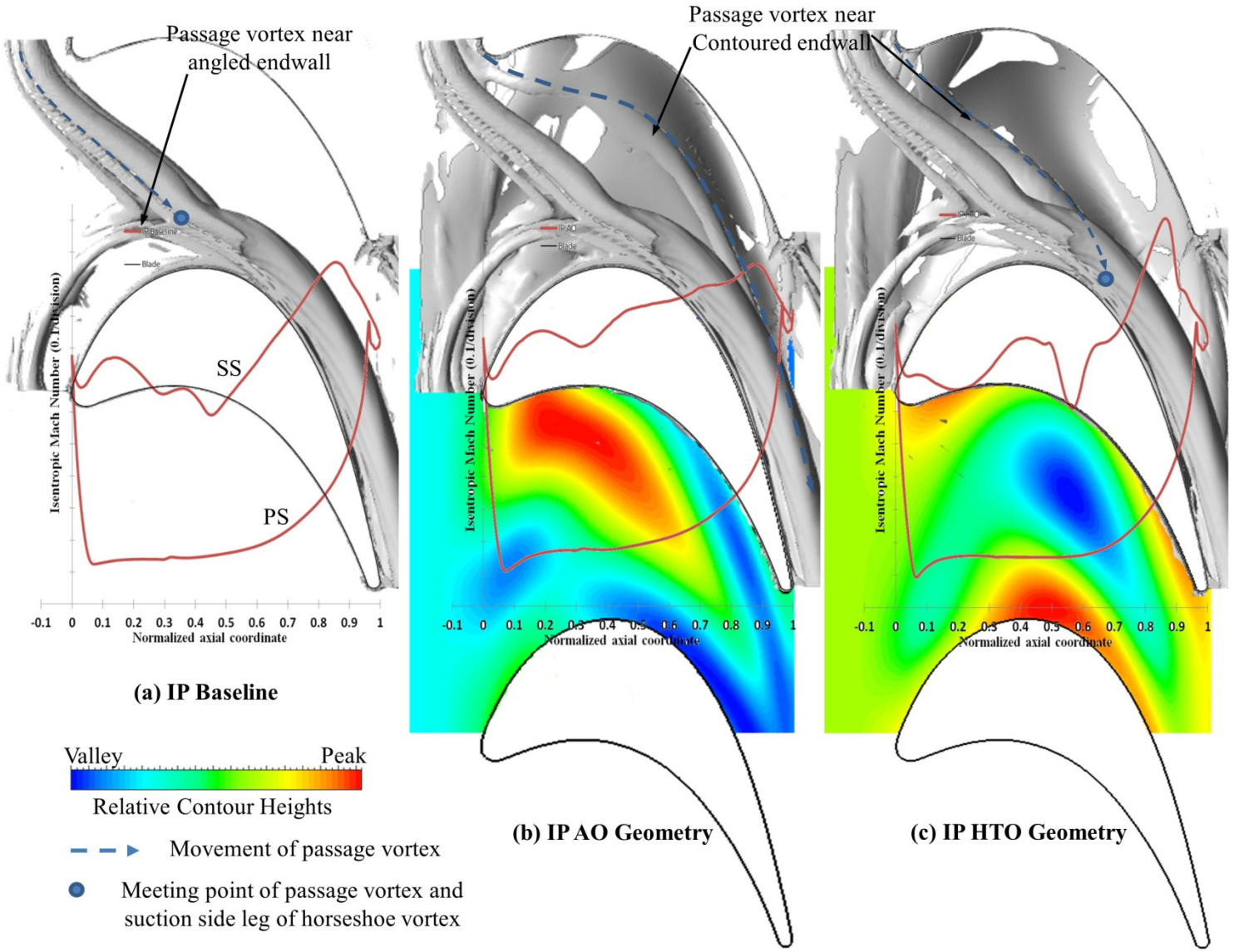

Figure 23 : Comparison of IP Endwall Contours, Blade Loading and Secondary Flow Formation

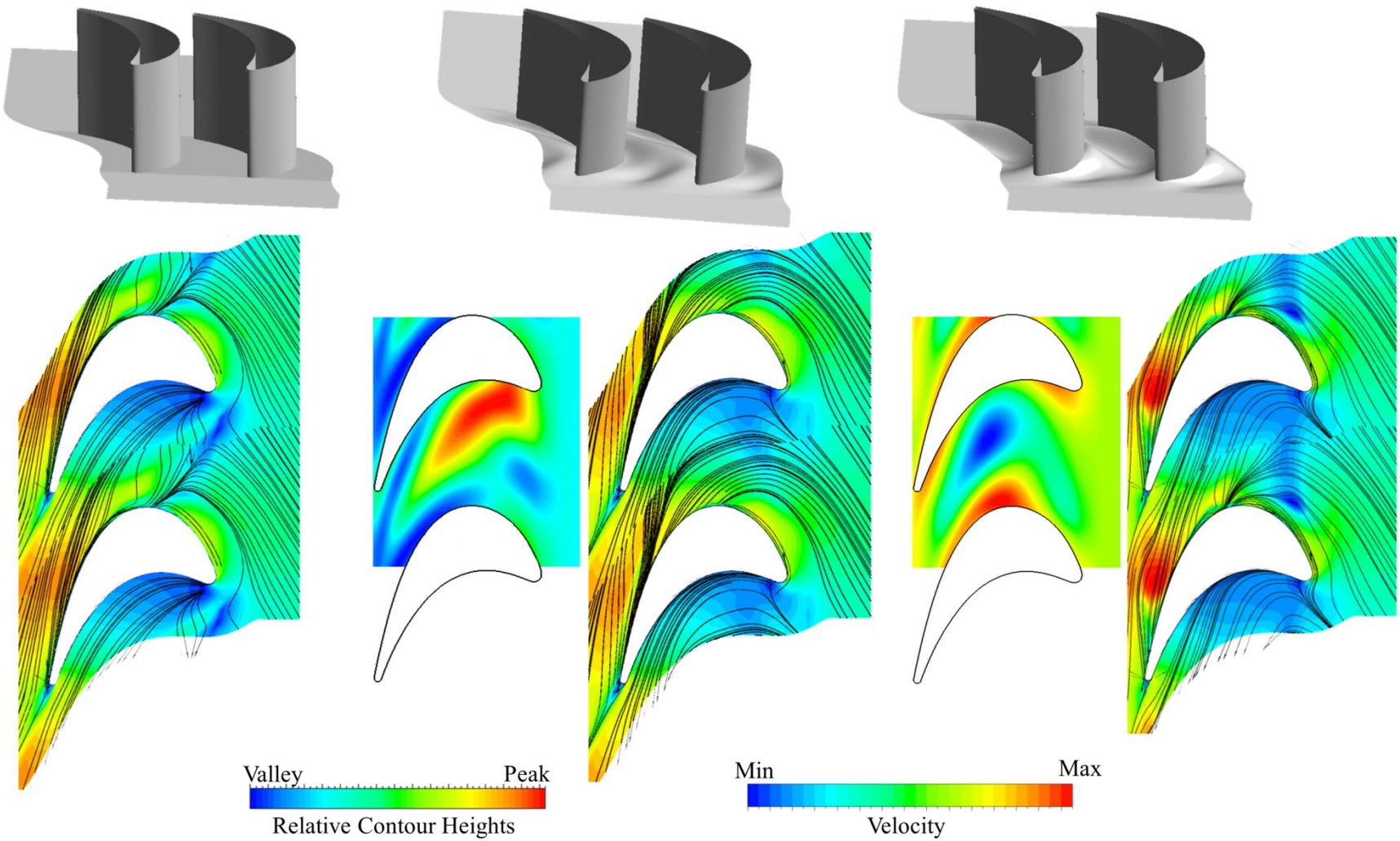

Figure 24 : Comparison of IP Endwall Contours and Velocity Profiles

Figure 25 shows the loss contours for all the IP geometries at $1.1\ C_{ax}$ location. The baseline geometry shows strong secondary flow with distinguished passage and counter vortex. The AO geometry shows that the passage vortex runs along the endwall whereas the wall vortex on the suction side develops as before. This reduces the strength of the wall vortex to some extent and avoids the mixing losses where the passage vortex meets the suction side leg of the horseshoe vortex.

It was observed that at the $0.99\ C_{ax}$ axial location, the product of loss coefficient and mass flow in the secondary region is about 52% of that for the whole area for the IP baseline case. However, the mass contained in the secondary flow region is only about 14.5% of the total mass flow. Similarly, the product of loss coefficient and mass flow in the secondary flow region is about 39% for the AO geometry. However, the mass contained in the secondary flow region is only about 11.5%. Therefore the net mass averaged reduction in the total pressure is a small value of about 4% at $2.0\ C_{ax}$ location.

The HTO geometry does not avoid the meeting point of the suction side leg of the horseshoe vortex. However, it does move this meeting point farther downstream. It was found that the product of loss coefficient and mass flow in the secondary flow region is about 50% of that for the area at $0.99\ C_{ax}$ location. The mass contained in the secondary flow region is about 12.5% of the total mass flow. Hence, the HTO geometry showed about 3% reduction in mass averaged loss coefficient at $2.0\ C_{ax}$ downstream location.

This shows that as the mass contained in the secondary flow region is a small fraction of the total mass flow for the whole area. Therefore, the reduction in mass averaged total pressure loss for such high speed flow turbine passage is not significant. The next chapter investigates the effect of endwall contouring on the heat transfer performance of the IP geometries.

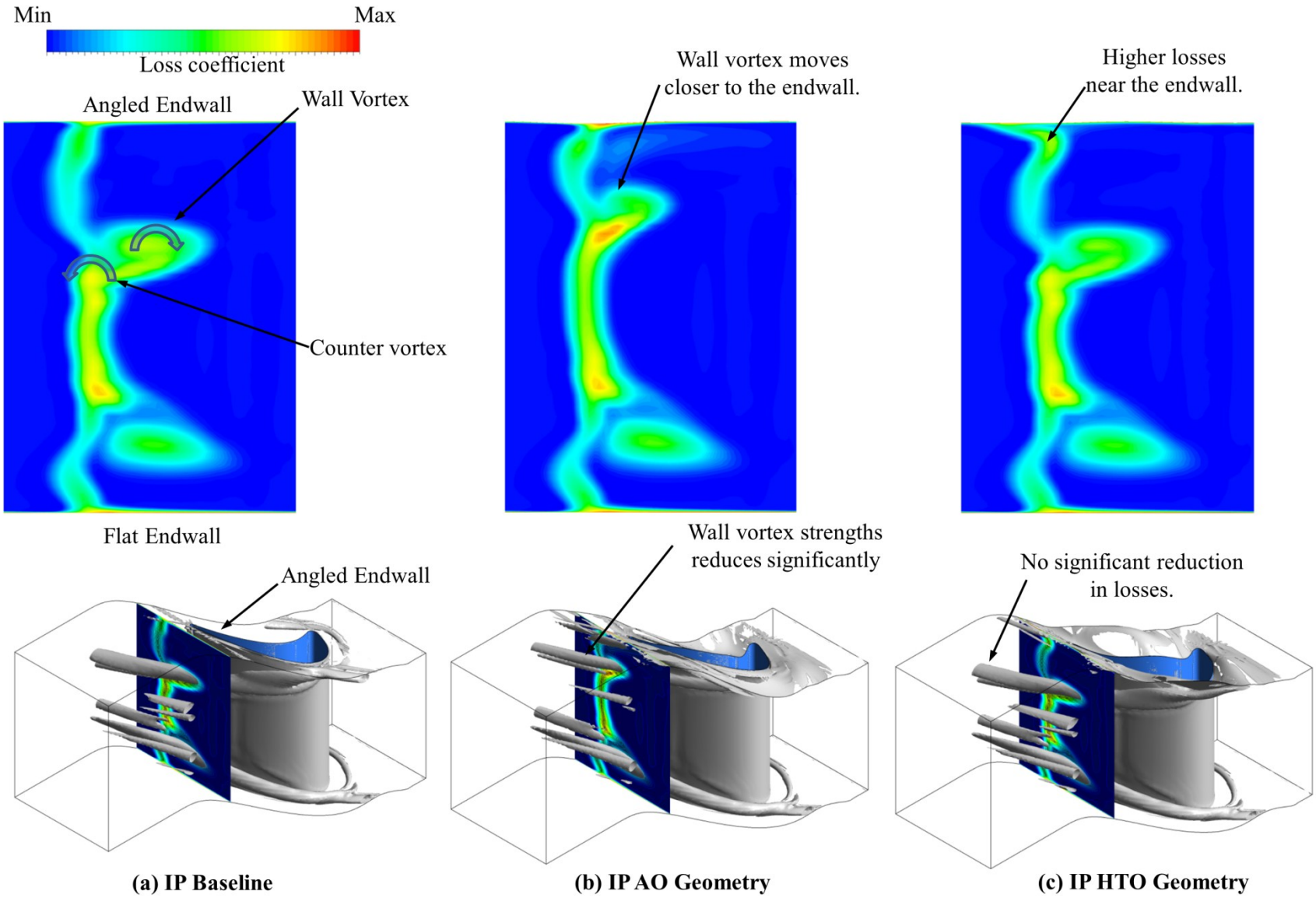

Figure 25 : Comparison of Loss Profiles at 1.1 C_{ax} Location for IP Endwall Geometries

7. Effect of Endwall Contouring on Heat Transfer Performance of the Turbine Passage

7.1 Overview

Investigation of effect of endwall contouring on heat transfer performance has not been studied much till date. Mohammad and Acharya [30] studied effect of endwall and leading edge modifications on the endwall heat transfer. However, these experiments were done at a very low Mach number of about 0.3. Lynch et al [31] studied the effect of endwall contouring on heat transfer performance of an LP turbine passage. Therefore the studies were done at a very low Mach number of 0.04. The reported area average reduction in heat transfer was of about 3%. However, till date no study is available in published literature that investigates the effect of endwall contouring on heat transfer performance of a turbine passage with high exit Mach number in transonic range.

This chapter describes the experimental heat transfer performance study for the IP baseline as well as the AO and HTO endwall geometries. Heat transfer measurements were carried out at three different Mach numbers (0.71, 0.88 and 0.95) for the baseline (non-contoured) as well as the other two contoured endwall geometries. Temperature measurements on the endwall were carried out using infrared thermography. The temperature data was then converted to HTC values and a comparative analysis was carried out.

Comparative study indicated that endwall contouring results in a significant reduction in overall average HTC values on the endwall. The improvement in heat transfer performance was similar for both the aero-optimized and the heat transfer optimized endwalls. However, unlike HTO endwall, the AO endwall provided slightly better aerodynamic performance improvement. The contoured endwall showed locally increased HTC values in a small area near leading edge and near the aft portion of the PS – endwall junction.

7.2 Experimental Test Facility

Figure 26 below shows a schematic of the Virginia Tech transonic linear cascade tunnel facility. This blow down facility is capable for both the aerodynamic as well as heat transfer

studies and has about 20 seconds of run time. The pressurized air is supplied to the tunnel by a four-stage Ingersoll-Rand compressor and stored in large outdoor tanks. The maximum tank pressure used for transonic tests is about 2068 kPa (300psig). Valve 1 regulates the flow of the air from the tanks to the test section. A computerized open loop system controls the opening of the valve in order to maintain the required test section total pressure during a run. There is another safety valve upstream of valve 1 that is used to start and stop the tunnel.

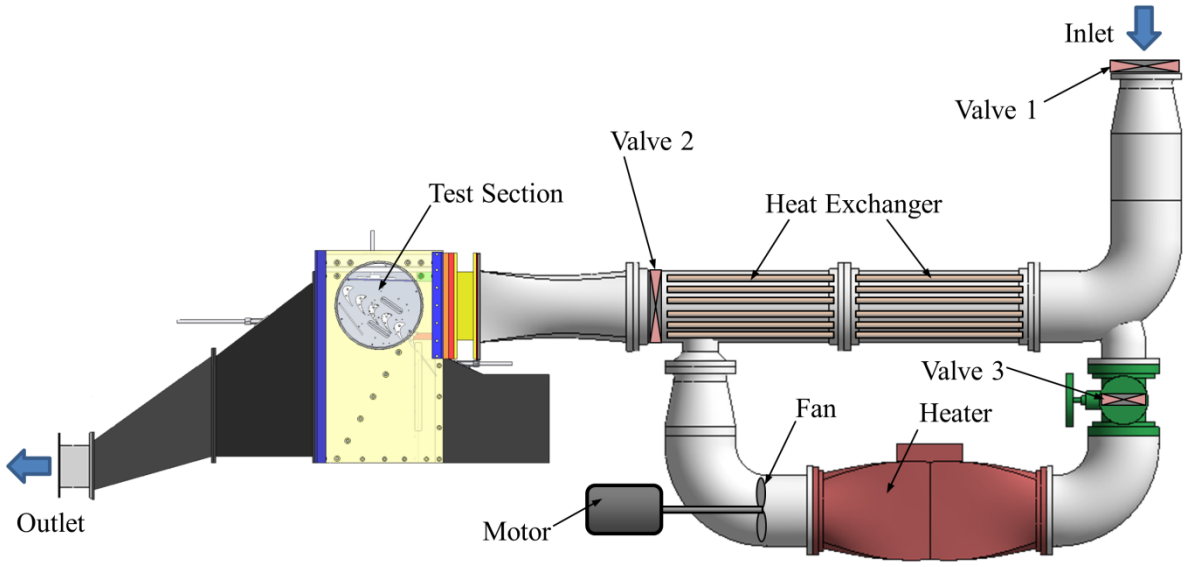

Figure 26: Virginia Tech transonic cascade wind tunnel

During a run, the upstream total pressure is maintained constant by varying the opening of the valve through computer controlled operation.

The airflow through the cascade is controlled by three valves, one at the inlet of the cascade, second valve just before test section inlet and the third valve in the heater section as shown in Figure 26. The first and the second valve remain open during the aerodynamic measurements while the third one remains closed allowing the air flow directly from inlet to the test section. For the heat transfer experiments, the valves one and two are initially kept closed and the third valve is kept open. Air is circulated through the heater and the heat exchanger. The heated air from heater heats up the copper tubes in the heat exchanger. The third valve is closed and the other two valves are opened when the temperature in the heat exchanger reaches a specified magnitude

(200 ^{o}F). The air gets heated through the heat exchanger while passing from the inlet to the test section.

The cascade test section, as shown in Figure 27 on the next page, consists of 6 airfoils resulting in 5 passages. The airfoils are mounted on a rotatable window, which allows for changes in incidence angles as and when required. A head board is used to control the bleed mass flow rate while the tail board is used to guide the exit flow. The flow starts turning much before the leading edge of the airfoil for such high turning passages. Therefore, the correct incidence angle of the incoming flow is achieved by adjustment of bleed flow by changing the head board angle and rotation of the window. The same method is used to ensure periodic flow in the cascade passages. The inlet Mach number is measured by a pitot static probe located 0.5 axial chords upstream of the center blade leading edge. The isentropic exit Mach number is decided based on the inlet total pressure and the average wall static pressure measured 0.5 axial chords downstream of the cascade. The airfoil isentropic exit Mach number is varied by changing the upstream total pressure.

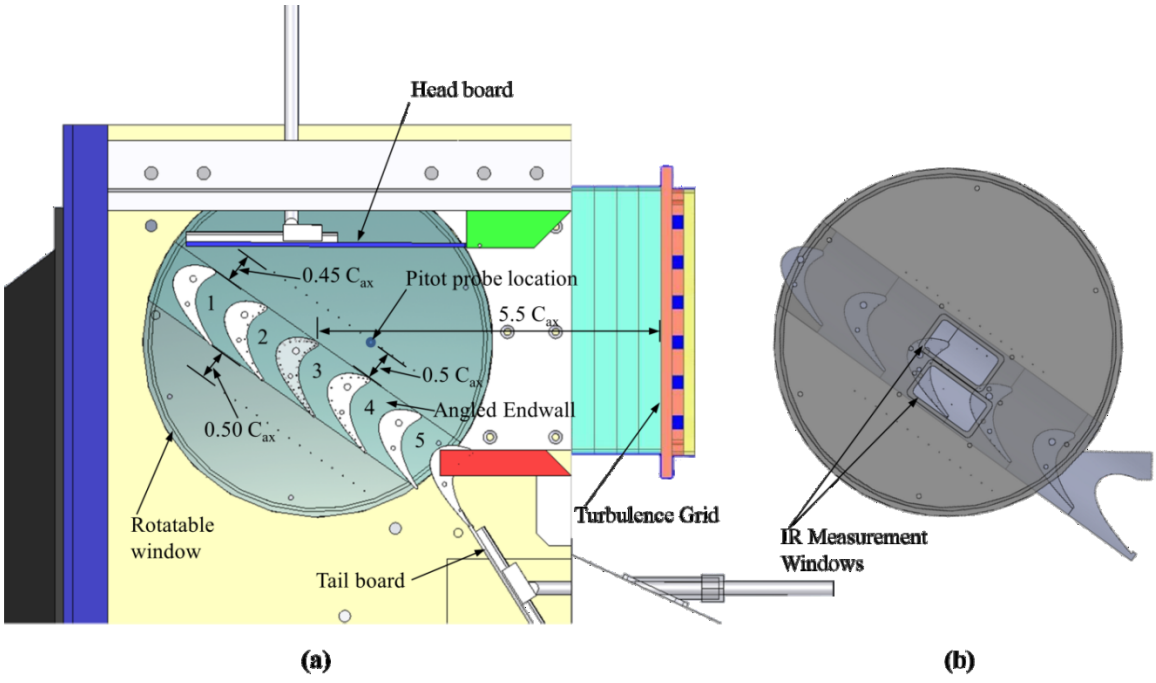

Figure 27: (a) Test section (b) IR Measurement Window

The rotatable window includes two rectangular slots for placement of the IR measurement windows during the heat transfer runs (Figure 27 (b)). Only one IR window is used at a time while the other window is kept closed.

7.3 Experimental Measurement Technique

The existing transonic cascade tunnel is a transient facility. During the heat transfer runs, the air coming to the test section has a temperature of about 93^{o}C as it passes through the heated copper tube heat exchanger. As more air passes through the heated pipes during the tunnel run time, the temperature of the heat exchanger pipes and therefore the temperature of the incoming air gradually decrease. However, for about a 5 second period the flow is aerodynamically steady. The cascade inlet temperature history is plotted in Figure 28 below.

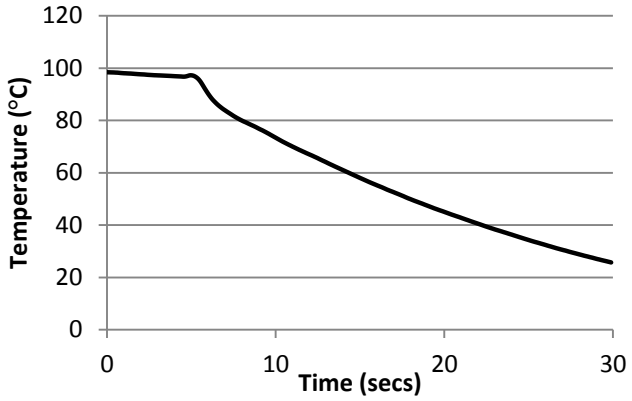

Figure 28 : Cascade Inlet Temperature History

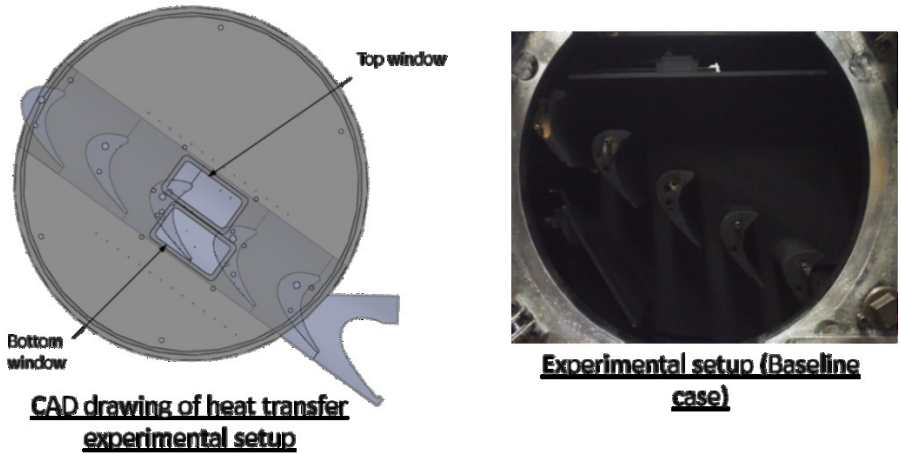

Figure 29: Heat transfer experimental setup

All the internal surfaces of the cascade were painted with a thin flat black paint coat in order to increase the emissivity of the surfaces and reduce the reflected radiation from the metallic surfaces. The endwall temperature measurements are made using FLIR SC325 IR camera. The measurements are taken with 320 X 240 pixel image resolution at 10Hz recording speed. In order to make temperature measurements using the IR camera, two 4.5 inch X 2.5 inch window slots are provided on the rotatable window. Two windows slots, instead of one, were used to cover the whole endwall due to mechanical and economic constraints. However, during a particular run only one window slot is used whereas the other slot is kept closed using a piece of Lexan. The slot houses a rectangular Zinc Selenide IR window of the same size. The IR window has a very high transmissivity of 0.97 in order to minimize the absorption of radiation coming to the IR camera. During each setup change thermocouples were placed in situ for IR camera calibration purpose.

Endwall temperature measurements were carried out for the baseline (non-contoured) case as well as two contoured endwall geometries at three different Mach numbers 0.71, 0.88 (design) and 0.95. For each Mach number, geometry, and IR window, the experimental runs were repeated multiple times to ensure repeatability of the results. The heat transfer coefficient (HTC) results were found to be repeatable within the range uncertainty with most results repeating with a difference of about 1-2%. The uncertainty in the calculation of HTC values was calculated to be about ±9.5%. The methodology for calculation of HTC values from available temperature history and the methodology for relating the 2D camera image matrix to the real world contoured/non-contoured endwall coordinates are discussed in the ensuing section.

7.4 Theory and data-reduction

7.4.1 Theory

The Acrylonitrile Butadiene Styrene (ABS) material was used to manufacture the turbine passages using rapid prototyping machine. ABS has a very low thermal conductivity. The temperature measurement window is a short time period of about 5 seconds. This results into a penetration depth $\sqrt{\alpha t}$ of about 0.8 mm for the data acquisition. Additionally, the flat black paint coating is very thin and the heat conduction in transverse direction can be considered to be negligible. Hence, the assumption of one dimensional semi-infinite heat transfer case can be

applied at every location on the endwall. Moreover, the tunnel is allowed to cool down for a significant amount of time between the two consecutive runs and therefore the whole endwall can be considered initially at a uniform temperature. As mentioned before, the infrared camera, ThermaCam SC325, has an image resolution of 320x240 giving temperature data at 76800 pixel locations. Due to the assumption of semi-infinite heat transfer case, the governing equation can be individually applied at each location.

The governing equation for the 1-D semi-infinite heat transfer is given by [32],

$$\frac{T_w - T_i}{T_m - T_i} = 1 - exp\left(\frac{h^2 \propto t}{k^2}\right) erfc\left(\frac{h\sqrt{(\propto t)}}{k}\right)$$

The mainstream temperature T_m is available from the temperature-time history of tunnel run. The IR camera image, just before the image where the temperature change on the endwall is observed, is considered as the initial temperatureT_i. The other values of material properties for ABS are also known. The IR camera images for the tunnel run provide variation of wall temperature T_w at each time step. As all the other quantities in the above equation are known, the value of heat transfer coefficient h at a given pixel location can be calculated.

7.4.2 Infrared Data Reduction Matlab Method

In order to solve the above equation for h, the value of h remains the same at a given pixel location for the duration of tunnel run time. The data reduction time period is about 5 seconds. The time history of the main stream temperature and the endwall temperature are available. An example of change in endwall temperature during the tunnel run time is shown in Figure 30 below.

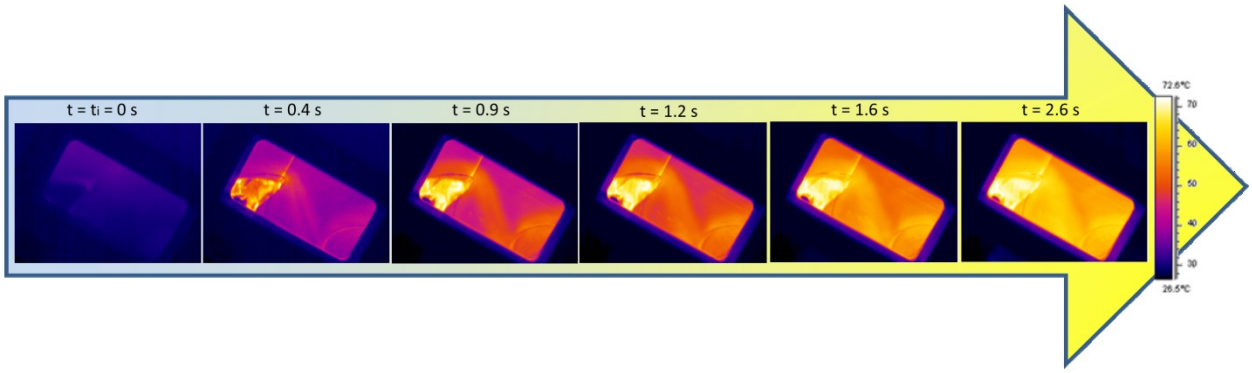

Figure 30 : Temperature variation during a typical tunnel run

Using this history of T_m and T_w data, one equation can be formed at each time step with only h being unknown. Such a data set is fitted to a curve using a Matlab program and the fminsearch function to minimize the error in curve fit. the measured wall temperature history is curve fit to the solution derived above using a Matlab program and the fminsearch function to minimize error in the curve fit. A sample curve fit is presented in Figure 31 below. Such a curve fit gives value of heat transfer coefficient.

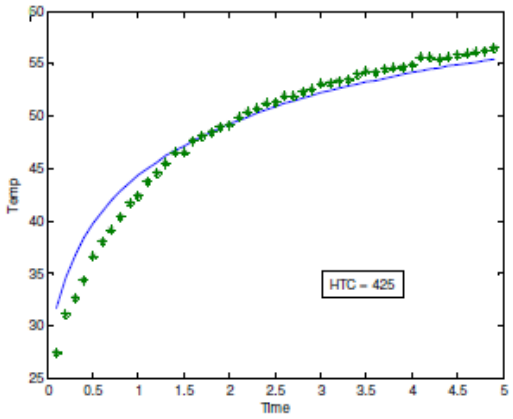

Figure 31 : Example curve fit of IR data

7.5 Uncertainty Analysis

The uncertainty values, based on the 1-D semi-infinite heat transfer model equation mentioned in the previous section, were calculated as below using Kline and McClintok's method [33].

The equation is $\frac{T_w - T_i}{T_m - T_i} = 1 - \left[\exp\left(\frac{h^2 \alpha t}{k^2}\right) erfc\left(\frac{h\sqrt{\alpha t}}{k}\right)\right]$ (1)

Hence, $h = f(T_w, T_i, T_m, \alpha, k, t)$

At a given time, T_w, T_i, T_m are not functions of time, they are constant.

Let (1) be written as $\frac{T_w - T_i}{T_m - T_i} = 1 - f(x)$, and

$$f(x) = \left[\exp\left(\frac{h^2 \alpha t}{k^2}\right) erfc\left(\frac{h\sqrt{\alpha t}}{k}\right)\right] = [\exp(x^2)\, erfc(x)]$$

Then $\frac{\partial h}{\partial T_w} = \frac{1}{\left(\frac{\partial T_w}{\partial h}\right)} = \frac{1}{\left(\frac{\partial T_w}{\partial x}\frac{\partial x}{\partial h}\right)}$ (2)

$\frac{\partial T_w}{\partial x} = -(T_m - T_i) f'(x)$

$\frac{\partial x}{\partial h} = \frac{\sqrt{\alpha} t}{k}$

From $\frac{T_w - T_i}{T_m - T_i} = 1 - f(x) \Rightarrow T_m - T_i = \frac{T_m - T_w}{f(x)}$

Hence, $\frac{\partial T_i}{\partial x} = \frac{T_m - T_w}{(f(x))^2} f'(x)$ and $\frac{\partial T_m}{\partial x} = -T_i \frac{1}{(1-f(x))^2} f'(x)$

$f'(x) = 2x \exp(x^2)\, erfc(x) + \exp(x^2) \frac{d(erfc(x))}{dx}$

Now, $\frac{d(erfc(x))}{dx} = -\frac{2}{\sqrt{\pi}} e^{-x^2}$, which gives,

$$f'(x) = \left(2x\, f(x) - \frac{2}{\sqrt{\pi}}\right) \quad (3)$$

$\frac{h^2 \alpha t}{k^2} = constant$. Hence, $\frac{\partial h}{\partial \alpha} = -\frac{h}{2\alpha}$ and $\frac{\partial h}{\partial t} = -\frac{h}{2t}$ and $\frac{\partial h}{\partial k} = \frac{h}{k}$

$$\frac{w_h}{h} = \left[\left(\frac{\partial h}{\partial T_w} w_{T_w}\right)^2 + \left(\frac{\partial h}{\partial T_m} w_{T_m}\right)^2 + \left(\frac{\partial h}{\partial T_i} w_{T_i}\right)^2 + \left(\frac{\partial h}{\partial \alpha} w_\alpha\right)^2 + \left(\frac{\partial h}{\partial k} w_k\right)^2 + \left(\frac{\partial h}{\partial t} w_t\right)^2\right]^{\frac{1}{2}} \quad (4)$$

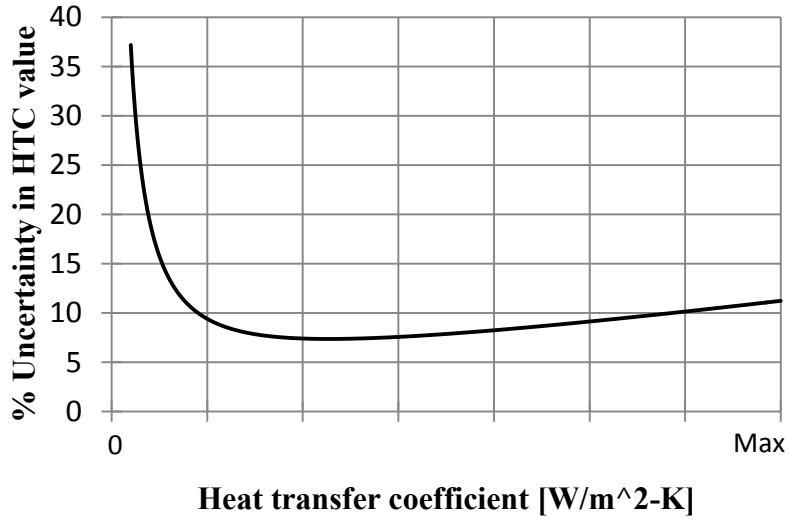

Figure 32 : Uncertainty in HTC Values

The above plot shows variation of percentage uncertainty $\left(\frac{w_h}{h}100\right)$ as a function of heat transfer coefficient. The average uncertainty in the range of HTC encountered for this case is about ±9.5 %. It may be noted that this uncertainty calculation method is to be used for single sample experiments. In the present study, multiple repeatability tests were performed and the observed uncertainty is considerably lower than the above prediction.

7.6 Post-processing of experimental results

The temperature history data on the endwall and for the mainstream temperature is used in the Matlab^{TM} routine to get the heat transfer coefficient (HTC) data matrix. Samples plots of such HTC data matrices for the top and the bottom window are shown in Figure 33(c). In order to have a better judgment of the heat transfer performance and to quantify the comparative effect of different geometries and flow conditions, both the top and the bottom window data needs to be stitched together. Moreover, the image pixel coordinates need to be related to the real world geometric coordinates in order to analyze the local heat transfer performance. The methodology used for identifying such relationship should also account for the fact that the image captured by the camera involves camera shear and perspective projection effects.

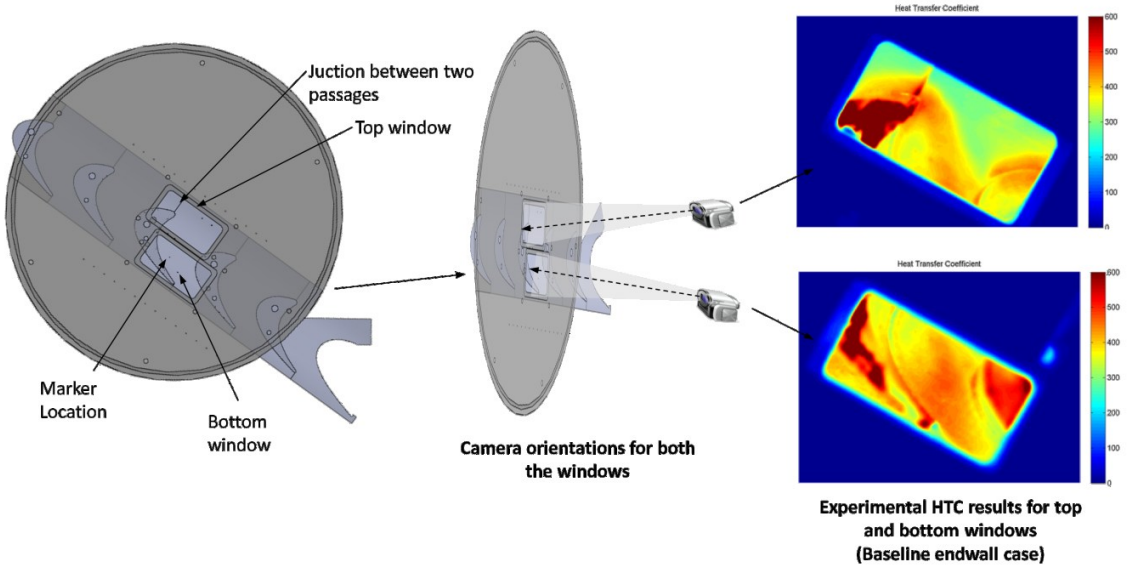

Figure 33 : (a) Front view of the experimental setup with IR window [left] (b) example of camera orientations for data acquisition through the top and the bottom windows [center] (c) Sample plots of HTC data for the top and the bottom windows[right].

Many marker locations were positioned on the endwall as shown in Figure 33(a). Real world coordinates of these locations are known. A small aluminum tape piece of about 0.5 mm x 0.5 mm is placed at each marker locations. Hence, these markers are distinctly visible in the temperature plots. The pixel coordinates of these markers are identified in the plots. In this way, we have a set of real world coordinates, X_R, and a corresponding set of maker pixel locations X_s. They are related through a camera matrix using a pin-hole camera model [34; 35; 36]. The following equation shows the relation between real-world coordinates and marker pixel coordinates.

$$[X_s]_{3\times n} = [M]_{3\times 4}\,[X_R]_{4\times n}$$

Here n is the number of marker locations. Larger the number of marker locations, more accurate is the camera matrix$M$. Once the camera matrix M is available, it can be used to relate any real world coordinate to corresponding marker pixel coordinate. HTC data was extracted for a large number of endwall coordinates distributed over a rectangular grid as shown in Figure 34(c). The same procedure is repeated for the bottom window for the same grid and then both the top and the bottom window data are combined. Due to highly repeatable data, the HTC values in the overlap region were the average values of the top and the bottom window data.

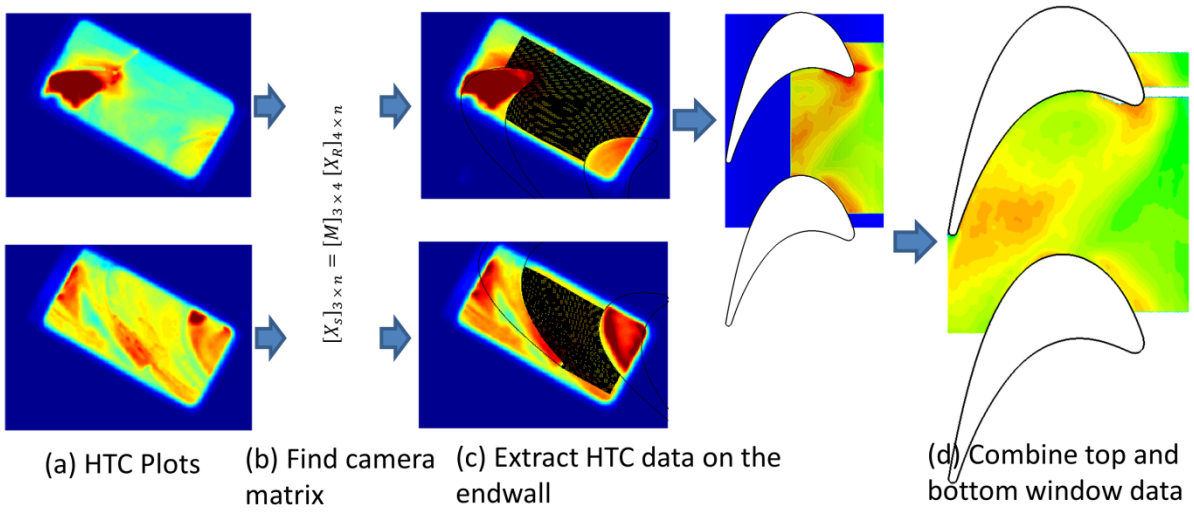

Figure 34 : HTC Data Extraction and Post-processing

Once the data for the whole endwall is available, the HTC data at the junction of two passages, see Figure 33(a) and Figure 34(d) is removed due to higher inaccuracy of HTC values.

7.7 Results and discussion

7.7.1 Overview

Three different endwall designs were studied for heat transfer performance investigations. The first endwall is a non-contoured (baseline) endwall. The other two endwalls are contoured endwalls of which one was obtained with an aim to optimize aerodynamic performance whereas the other was obtained with an aim to optimize heat transfer performance. The details of experimental measurement methodology are discussed in Part 1 of this study.

The heights of the endwall contours are as shown in the figure below. It may be noted that the aero optimized geometry exhibits a strong peak region near the pressure side in the front region of the passage whereas the heat transfer optimized geometry shows a deep trough in the middle passage region.

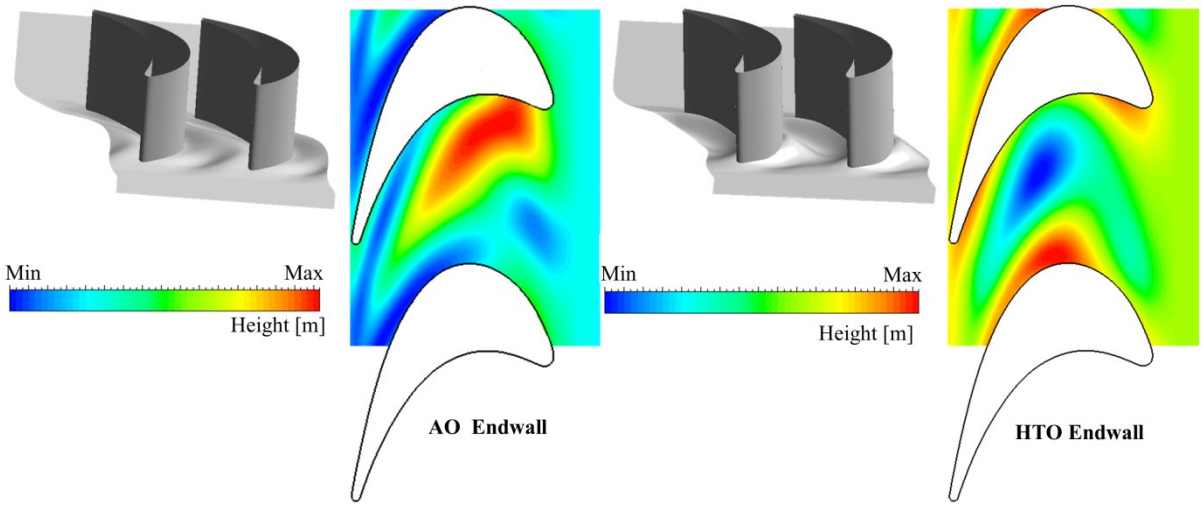

Figure 35 : Contour heights for endwall geometries

All the experiments for both the top and the bottom window locations were conducted multiple times to ensure repeatability. All the cases were found to be repeatable within a range of 0.5-6% of local HTC values. However for most runs the cases were repeatable within a range of

0.5-3%. These ranges are sufficiently smaller than the estimated uncertainty in the measurements.

Additionally, uniformity in upstream HTC values was measured for about 5 mm wide strip in the region from about $0.16C_{ax}$ to $0.22\,C_{ax}$ mm away from the leading edge. The HTC values were uniform with a standard deviation of about 5% of the average value.

7.7.2 Baseline Case (non-contoured endwall)

Figure 36 shows HTC value plots for the baseline endwall at three different Mach numbers. The baseline area average (on the area shown in the figure) HTC value is considered as the reference value and the relative performance at off-design Mach numbers and for different geometries is evaluated. It was observed that the average HTC values were about 10% higher for the Mach number 0.95 than that for the design Mach number of 0.88. The M=0.71 case showed about 16% lower average HTC values. The highest HTC values were observed in the near leading edge region where the flow velocities are low.

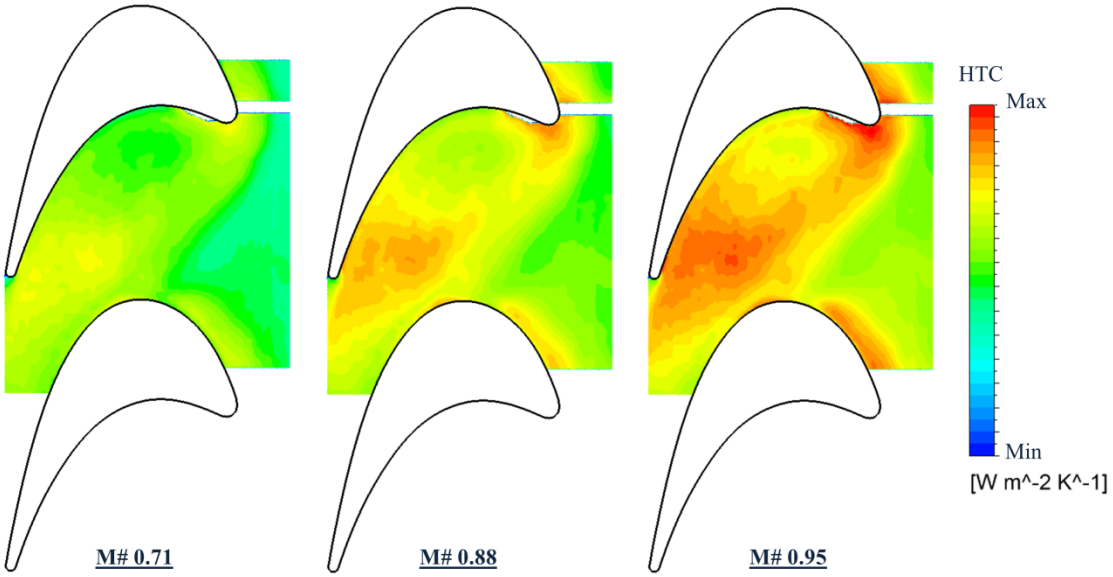

Figure 36 : Heat transfer performance of the baseline endwall at different Mach numbers

Figure 37 shows vortex core regions obtained from the results of CFD analysis superimposed on the experimental HTC results for the design Mach number case. It can be seen that the V shaped pattern observed in the upstream region of HTC plots is the result of the passage vortex and suction side leg of the horseshoe vortex.

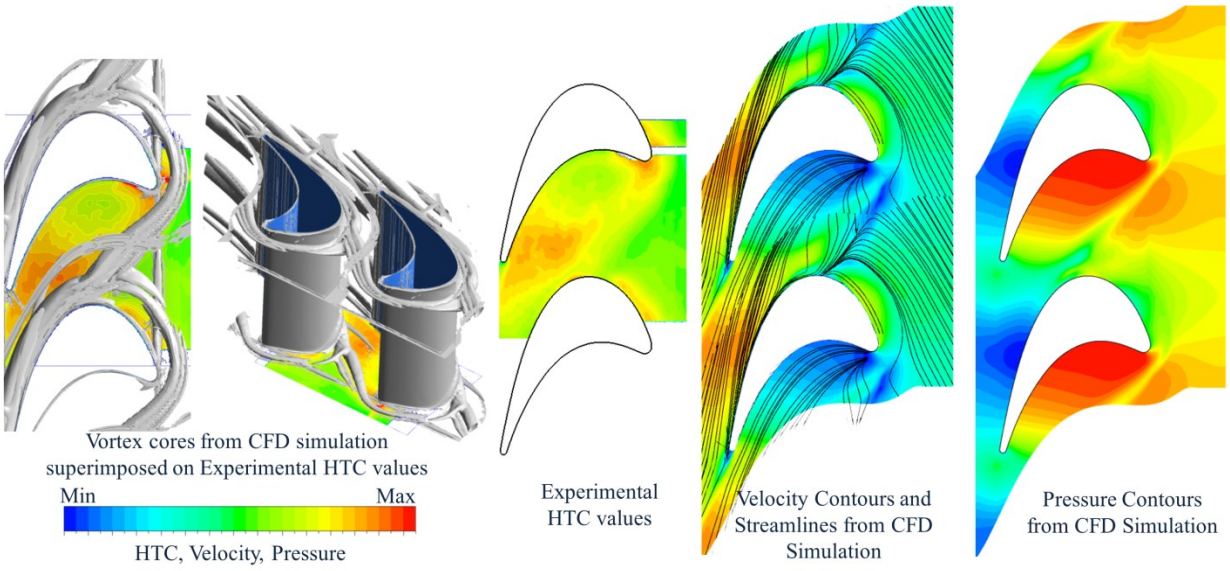

Figure 37 : Superimposition of vortex cores (CFD results) on the experimental HTC data for the baseline case

The velocity contours clearly show high velocity region on the path of the passage vortex. This results into higher heat transfer coefficient values. In the area near the throat the velocity increases rapidly resulting into higher heat transfer coefficients in the near throat region.

7.7.3 Aero-Optimized Endwall

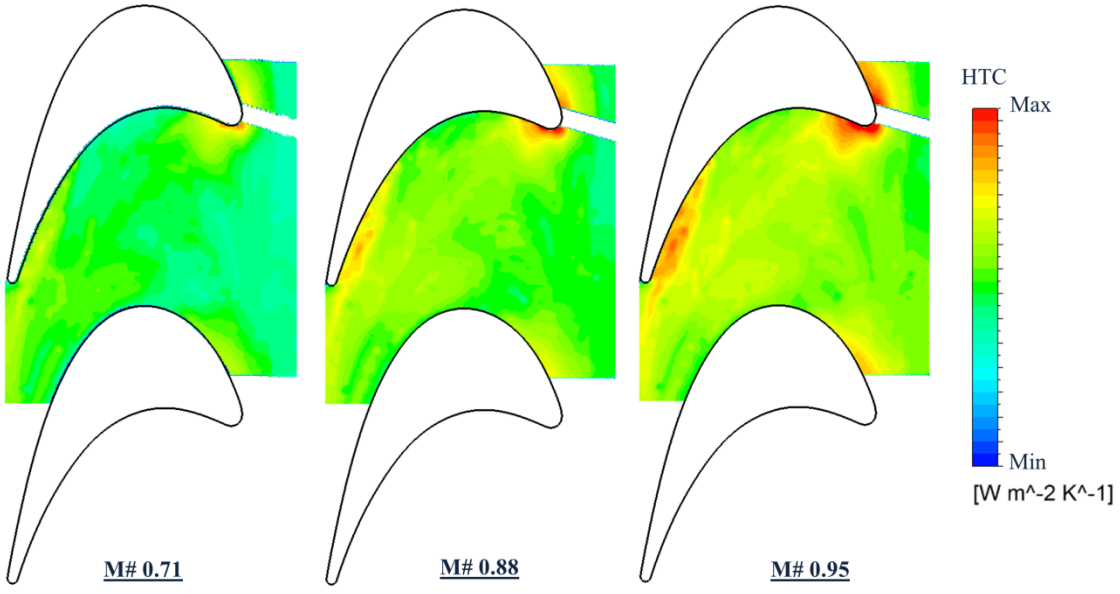

Figure 38: Heat transfer performance of the AO endwall at different Mach numbers

Figure 38 shows HTC distribution over the AO contoured endwall. The comparison between Figure 36 and Figure 38 shows clear reduction of HTC value over the whole endwall. However, the local HTC values near the leading edge and in the pressure side aft region were obseved to be higher than the baseline case values at the same location.

The area averaged HTC value was found to be about 11.3% lower for Mach number 0.71 than that for the design Mach number. The area averaged HTC was about 10% higher for Mach number 0.95 than that for the design Mach number. These numbers are similar to the corresponding numbers for the baseline case.

Superimposition of vortex cores from CFD results on the experimental results shows that the endwall contouring breaks the horseshoe vortex and reduces its strength. Also it avoids the meeting point of the passage vortex and the suction side leg of the horseshoe vortex up to a longer length. These changes in the strength and direction of the vortex structure (see Figure 39) near the endwall result into overall lower average values for the AO endwall case as compared to the baseline case. The flow structure near the opposite non-contoured endwall remains unchanged.

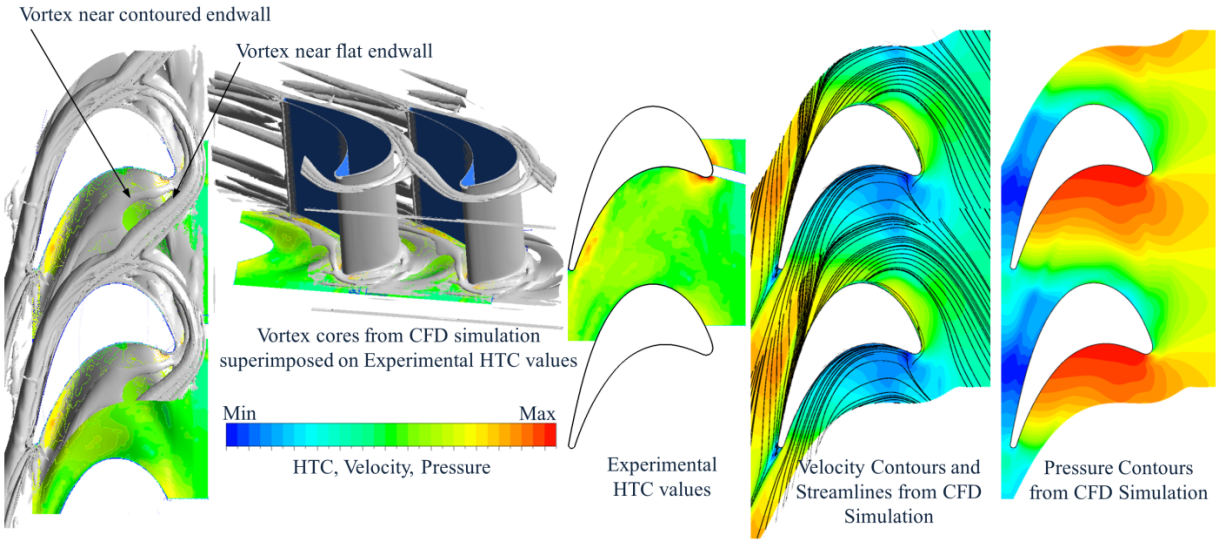

Figure 39 : Superimposition of vortex cores (CFD results) on the experimental HTC data for the AO endwall

7.7.4 Heat Transfer Optimized Endwall

Figure 40 shows HTC distribution over the HTO contoured endwall. The comparison between Figure 36 and Figure 40 shows clear reduction of HTC value over the whole endwall. However,

the local HTC values near the leading edge and in the pressure side aft region were obseved to be higher than the baseline case values at the same location . This was also observed in the AO endwall case.

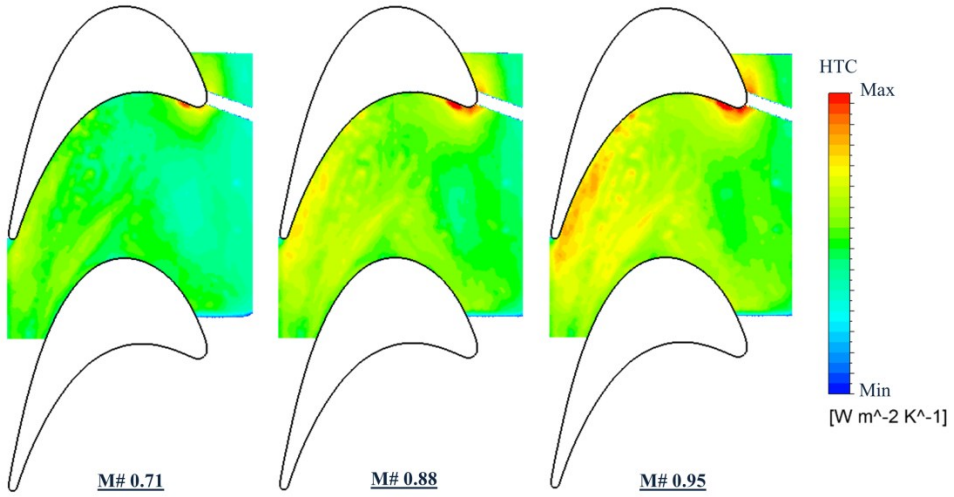

Figure 40 : Heat transfer performance of the HTO endwall at different Mach numbers

The area averaged HTC value was found to be about 13.4% lower for Mach number 0.71 than that for the design Mach number. The area averaged HTC was about 7.2% higher for Mach number 0.95 than that for the design Mach number. These numbers are similar to the corresponding numbers for the baseline case.

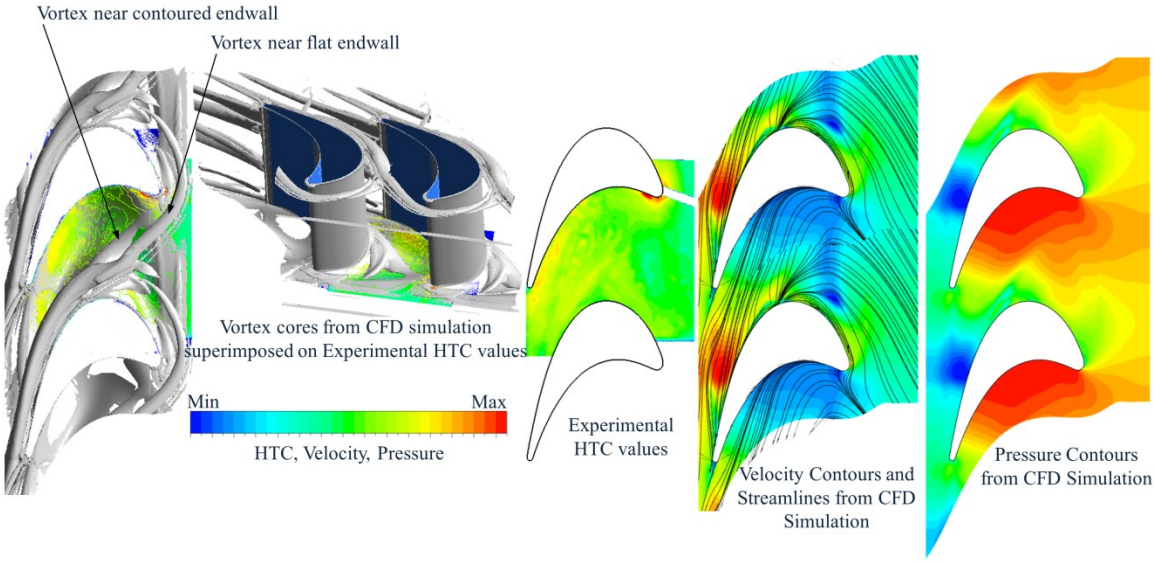

Figure 41 : Superimposition of vortex cores (CFD results) on the experimental HTC data for the HTO endwall

Superimposition of vortex cores from CFD results on the experimental results shows that the endwall contouring breaks the horseshoe vortex and reduces its strength. These changes in the strength and direction of the vortex structure (see Figure 41) near the endwall result into overall lower average values for the HTO endwall case as compared to the baseline case. The flow structure near the opposite non-contoured endwall remains unchanged.

7.7.5 Comparative Performance of the Endwalls

The table below shows comparative heat transfer performance of the different endwalls considering the baseline design case as a reference. The aero-optimized and the heat transfer optimized geometries show almost identical reduction in HTC values at design Mach numbers. The HTO geometry shows slightly higher reduction in the HTC values as compared to the AO geometry. However, this reduction is within the limit of experimental repeatability and is insignificant.

Table 3 : Change in average HTC value relative to the baseline design Mach number case

Geometry	M=0.71	M#0.88	M#0.95
Baseline geometry	-16%	Reference	+10%
Aero-optimized geometry	-27%	-15.7%	-6.8%
Heat transfer optimized geometry	-29%	-15.6%	-8.4%

Figure 42 shows plots of difference in HTC values between the contoured and the non-contoured (baseline) geometries for both the AO and the HTO endwalls. It can be seen that the major reduction in HTC values is achieved along the path of the passage vortex for the baseline endwall. However, both the contoured geometries show increased HTC values near the leading edge.

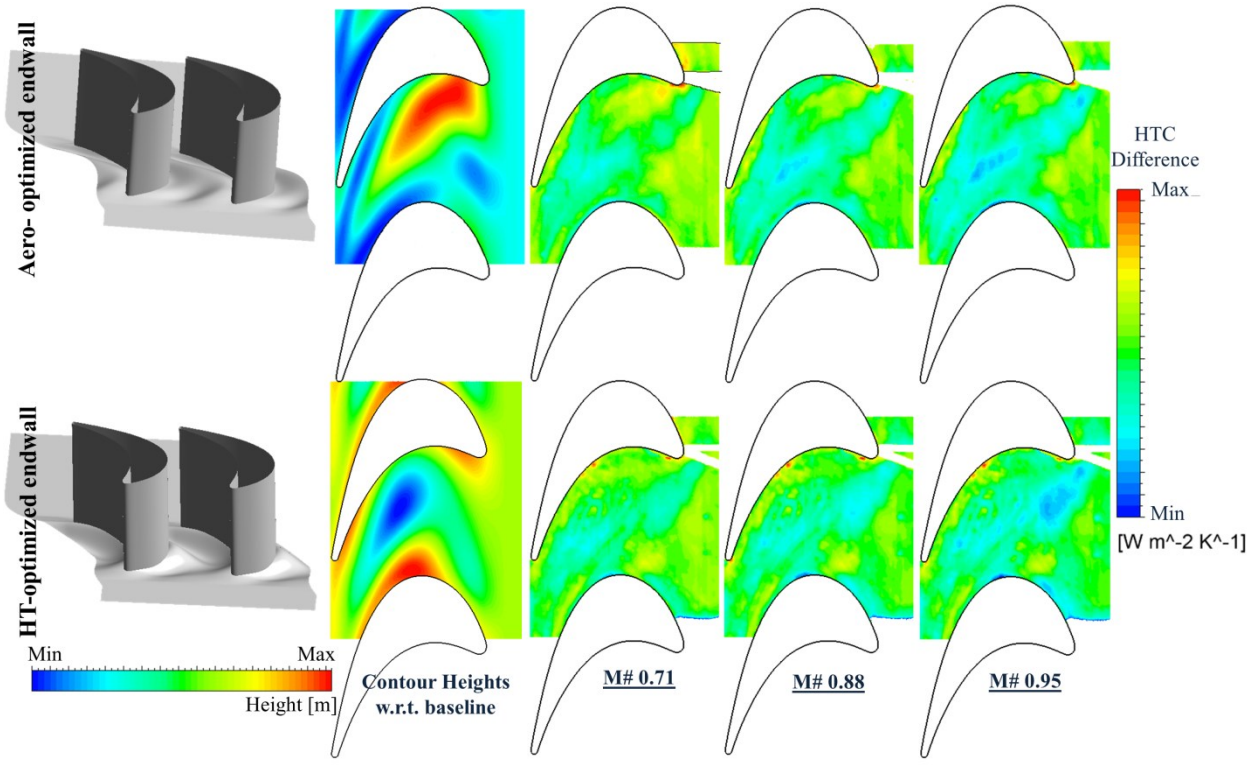

Figure 42 : Comparative performance of the endwalls

The results from the heat transfer study show that evidently the heat transfer performance can be greatly improved through endwall contouring.

8. Conclusions

Part I: Development of a robust numerical optimization methodology and its application to a transonic turbine blade passage.

A robust numerical optimization methodology for turbine endwall contouring has been developed. Unlike the existing tools, this methodology gives the designer more freedom and flexibility for the selection of the location of endwall control parameters and thereby reduces the optimization effort. The parameter value selection to the solution time was significantly reduced due to the use of automated direct mesh modification method.

This methodology was applied to a high turning, high exit Mach number transonic turbine blade passage to obtain an endwall contour geometry based on the aerodynamic performance optimization criterion. The blade profile was provided by the Siemens Energy, Inc. A contoured endwall was then obtained for a transonic turbine passage using this methodology. A second endwall contour geometry was obtained by normalizing a surface geometry shape obtained from literature. Additionally, a third geometry using the minimization of secondary kinetic energy (SKE) criterion was also studied. The following conclusions were observed from the study:

- The mass contained in the secondary flow region for such high speed flows is a small fraction of the mass averaged loss over the whole area. Hence, even a significant reduction in secondary losses will result in a small reduction in mass averaged stagnation pressure loss. Hence, the performance gain due to endwall contouring is expected to be small for such high speed, high turning turbine passages.

- It seems that the SKE is not the primary factor affecting the mass averaged total pressure losses. Endwall contouring was found to reduce the SKE to a near optimum value. Hence, a correct approach for the endwall contouring optimization is reduction in the mass averaged total pressure loss and not the reduction in the SKE values. However, it may be possible to achieve better flow distribution in front of the blade by contouring both the endwalls of vanes.

- The endwall contour shape is dependent on the loading distribution around the blade in addition to the other design parameters like aspect ratio, solidity, exit Mach number etc. Although the passage design parameters for two different passages may be similar, the exact location and the

height of the endwall contours are highly dependent on the blade loading distribution. Therefore, the endwall contouring requires optimization of the geometry on case by case bases.

- Analysis indicates that endwall contouring results in a small performance gain on this design due to its low predicted level of secondary and endwall losses. It is expected that for the designs with low aspect ratios, increased airfoil loading, more front loaded blades etc., where the secondary losses are a significant portion of total loss, endwall contouring may result in larger performance gains.

Part II: Effect of endwall contouring on a turbine passage with increased pitch

Based on the conclusions of the study described in Part I, three endwall designs with increased pitch were provided by Siemens Energy, Inc. Out of these, one geometry is the increased pitch non-contoured baseline design whereas the other two are contoured endwall geometries. One contoured endwall geometry was obtained based on the aerodynamic performance optimization criterion whereas the other geometry was obtained based on the heat transfer performance optimization criterion. Aerodynamic performance of the geometries was studied through numerical simulations.

Heat transfer performance of all the three geometries was experimentally investigated at three different Mach numbers (0.71, 0.88, and 0.95) using IR thermography technique in Virginia Tech transonic cascade tunnel facility.

- The increased pitch baseline showed a clear effect of horseshoe vortex on heat transfer performance resulting in high HTC values just downstream of the horseshoe vortex. The contoured endwalls (both AO and HTO) seem to mitigate and redirect the horseshoe vortex in order to reduce the HTC values in this region.
- For all the endwall geometries, the overall HTC values were observed to increase with increasing Mach number. However, the distinct HTC patterns over the endwall remained the same for a given geometry and the HTC values changed only in magnitude.
- Both the aero-optimized and the heat-transfer optimized endwalls showed a reduction in average HTC values by about 15.5% at the design conditions. However, the maximum HTC values were found to increase by about 10% in the leading edge region.
- It may be concluded that both the aero-optimized and the heat-transfer optimized geometries result into a significant performance improvement from the heat transfer performance point of view.

10. References

1. *Rotational flow through cascades.* Hawthorne, W. R. 1955, Jl. Mech. & Appl. Math., Vol. 3.
2. *Secondary Flows in Axial Turbines - A Review.* Langston, L. A. 2001, Annals of New York Academy of Sciences. 934.
3. *An experimental study of heat transfer and film cooling on low aspect ratio turbine nozzles.* Takeishi, K., et al. July 1990, ASME Journal of Turbomachinery, Vol. 112, pp. 488-496.
4. *Predictions of endwall losses and secondary flows in axial flow turbine cascades.* Sharma, O. P. and Butler, T. L. 1987, ASME Jl. of Turbomachinery, Vol. 109, pp. 248-257.
5. *Flow visualisation in a linear turbine cascade of high performance turbine blades.* Wang, H. P., et al. 1997, ASME Jl. of Turbobmachinery, Vol. 119, pp. 1-8.
6. *The influence of blade lean on turbine losses.* Harrison, S. 1992, ASME Jl. of Turbomachinery, Vol. 114, pp. 184-190.
7. *Influence of sweep on axial flow turbine aerodynamics at midspan.* Pullan, G. and Harvey, N. W. 2007, ASME Jl. of Turbomachinery, Vol. 128, pp. 591-598.
8. *Application of boundary fences in turbomachinery.* Prumper. 24. AGARD-CP-164. pp. 315-331. Paper No. II-3.
9. *Effectiveness of the gas turbine endwall fences in secondary flow control at elevated freestream turbulence levels.* Chung, J. T. and Simon, T. W. 1993. ASME Paper No. 93-GT-51.
10. *Secondary flow measurements in a turbine passage with endwall modification.* Aunapu, N. V., et al. 2000. ASME Paper No. 2000-GT-212.
11. *Reduction of secondary flow losses in turbine cascades by leading edge modifications at the endwall.* Sauer, H., Muller, R. and Vogeler, K. 2000. ASME Paper No. 2000-GT-473.
12. *Secondary losses and end-wall profiling in a turbine cascade.* Atkins, M. J. 1987. IMechE Paper No. C255/87.
13. *Controlling the secondary flow in a turbine cascade by three-dimensional airfoil design and endwall contouring.* Duden, A., Raab, I. and Fottner, L. 1999, ASME Jl. of Turbomachinery, Vol. 121, pp. 191-199.

14. *Experimentally verified numerical optimization of a 3D-parameterised turbine vane with non-axisymmetric endwalls.* Nagel, M. G. and Baier, R. D. Atlanta,Georgia,USA : s.n., 2003. Proceedings of ASME Turbo Expo 2003. GT2003-38624.

15. *Computations of turbulent flow and heat transfer through a three-dimensional non-axisymmetric blade passage.* Saha, A. K. and Acharya, S. Barcelona : s.n., 2006. ASME Turbo Expo 2006: Power for land, sea and air. Paper No. GT2006-90390.

16. *Application of non-axisymmetric endwall contouring to conventional and high-lift turbine airfoils.* Prisner, T. J., et al. Montreal : s.n., 2007. ASME Turbo Expo 2007: Power for Land,Sea and Air. Paper No. GT2007-27579.

17. *Nonaxisymmetric turbine endwall design: Part I-Three-dimensional linear design system.* Harvey, N. W., et al. 2000, ASME Journal of Turbomachinery, Vol. 122, pp. 278-285.

18. *Secondary loss measurements in a cascade of turbine blades with meridional wall profiling.* Morris, A. W. H. and Hoare, R. G. 1975. ASME Paper 75-W/GT-13.

19. *Experimental investigation of endwall profiling in a turbine vane cascade.* Kopper, F. C. and Milano, R. 8, August 1981, AIAA Jl., Vol. 19, pp. 1033-1040. AIAA 80-1089R.

20. *Non-axisymmetric endwall profiling in the HP NGV's of an axial flow gas turbine.* Rose, M. G. International gas turbine and aeroengine congress and exposition. 94-GT-249.

21. *Nonaxisymmetric turbine endwall design: Part II - Experimental validation.* Hartland, J. C., et al. April 2000, ASME Jl. of Turbomachinery, Vol. 122, pp. 286-293.

22. *A design method for the profiling of endwalls in turbines.* Hartland, J. and Gregory-Smith, D. G. Amstredam : s.n., 2002. Proceedings of ASME Turbo Expo 2002. GT-2002-30433.

23. *Experimentally verified numerical optimization of a three dimensional parameterized turbine vane with nonaxisymmetric endwalls.* Nagel, M. G. and Baier, R. D. April 2005, ASME Jl. of Turbomachinery, Vol. 127, pp. 380-387.

24. *Aerodynamic measurements in a linear turbine blade passage with three-dimensional endwall contouring.* Gustafson, R., Mahmood, G. and Acharya, S. Montreal : s.n., 2007. Proceedings of GT 2007, ASME Turbo Expo 2007. GT2007-28073.

25. *The application of non-axisymmetric endwall contouring in a single stage, rotating turbine.* Snedden, G., et al. Florida : s.n., 2009. Proceedings of GT2009, ASME Turbo Expo 2009: Power for land, sea and air. GT2009-59169.

26. *Application of endwall contouring to transonic turbine cascades: Expeirmental measurements at design conditions.* Taremi, F., Sjolander, S. A. and Praisner, T. J. Vancouver : ASME Turbo Expo 2011, 2011.

27. Piegl, L. A. and Tiller, W. *The NURBS book (Monographs in visual communication).* 2nd. New York : Springer, 1996. p. Chap. 9.

28. Oberkampf, W. L. and Roy, C. J. *Verification and validation in scientific computing.* Cambridge : Cambridge University Press, 2010.

29. *Investigation of effect of end wall contouring methods on a transonic turbine blade passage.* Panchal, K., et al. Vancouver : s.n., 2011. Proceedings of ASME Turbo Expo 2011. GT2011-45192.

30. *Measured endwall flow and heat transfer in a linear blade passage with endwall and leading edge modifications.* Mohammad, G. I. and Acharya, S. s.l. : ASME TurboExpo 2007, 2007. GT 2007 -28179.

31. *Heat transfer for a turbine blade with non-exisymmetric endwall contouring.* Lynch, S. P., et al. Florida : ASME TurboExpo 2009, 2009. GT 2009-60185.

32. Incropera, F. P., et al. *Fundamentals of heat and mass transfer.* 6th. s.l. : John Wiley & Sons, 2007.

33. *Describing uncertainties in single sample experiments.* Kline, S. J. and McClintok, F. A. 1953, Mechanical Engineering, pp. 3-8.

34. Sonka, M., Hlavac, V. and Boyle, R. *Image processing, analysis and machine vision.* s.l. : CL - Engineering, 2007. 3rd.

35. Schalkoff, R. J. *Digital image processing and computer vision.* International Edition. s.l. : John Wiley and Sons Ltd., 1989.

36. Pratt, W. K. *Digital Image Processing.* 4th. s.l. : Wiley Interscience, 2007.

Appendix A – Contribution of secondary losses

Effect of reduction in secondary losses on the reduction in mass averaged total pressure loss

The mass averaged loss is given by the formulae,

$$\omega_{Total} = \frac{\int L_{coe}\, d\dot{m}}{\dot{m}} \tag{1}$$

The numerator on the right hand side can be divided into two areas, one includes the secondary flow region (sec) and the other includes the rest(r). Hence,

$$\omega_{Total} = \frac{\int_{sec} L_{coe-sec}\, d\dot{m}}{\dot{m}} + \frac{\int_{r} L_{coe-r}\, d\dot{m}}{\dot{m}} \tag{2}$$

$$\Rightarrow \omega_{Total} = \frac{\dot{m}_{sec}}{\dot{m}} \frac{\int_{sec} L_{coe-sec}\, d\dot{m}}{\dot{m}_{sec}} + \left(1 - \frac{\dot{m}_{sec}}{\dot{m}}\right) \frac{\int_{r} L_{coe-r}\, d\dot{m}}{\dot{m} - \dot{m}_{sec}}$$

$$\Rightarrow \omega_{Total} = \frac{\dot{m}_{sec}}{\dot{m}} \omega_{sec} + \left(1 - \frac{\dot{m}_{sec}}{\dot{m}}\right) \omega_{r} \tag{3}$$

$$\Rightarrow \Delta\omega_{Total} = \frac{\dot{m}_{sec}}{\dot{m}} \Delta\omega_{sec} + \left(1 - \frac{\dot{m}_{sec}}{\dot{m}}\right) \Delta\omega_{r}$$

$$\Rightarrow \frac{\Delta\omega_{Total}}{\omega_{Total}} = \frac{\dot{m}_{sec}}{\dot{m}} \frac{\Delta\omega_{sec}}{\omega_{Total}} + \left(1 - \frac{\dot{m}_{sec}}{\dot{m}}\right) \frac{\Delta\omega_{r}}{\omega_{Total}}$$

$$\Rightarrow \frac{\Delta\omega_{Total}}{\omega_{Total}} = \frac{\dot{m}_{sec}}{\dot{m}} \frac{\omega_{sec}}{\omega_{Total}} \frac{\Delta\omega_{sec}}{\omega_{sec}} + \left(1 - \frac{\dot{m}_{sec}}{\dot{m}}\right) \frac{\omega_{r}}{\omega_{Total}} \frac{\Delta\omega_{r}}{\omega_{r}} \tag{4}$$

The equation (4) says that even a significant reduction in secondary losses will result in smaller changes in reduction in mass averaged total pressure loss if the product of mass flow rate and losses in secondary flow region are a small fraction of that for the entire area.

Appendix B – Fair Use Analysis Checklist and Results

Draft 08/31/2009

(Questions? Concerns? Contact Gail McMillan, Director of the Digital Library and Archives at Virginia Tech's University Libraries: gailmac@vt.edu)

(Please ensure that Javascript is enabled on your browser before using this tool.)

Virginia Tech ETD Fair Use Analysis Tool

Please complete all fields and answer all questions. You must answer every question to receive fair use determination guidance. If you answer "don't know," it will weigh against fair use.

Your name

Kapil Vitthalbhai Panchal

Provide a citation for the item you are considering for fair use: (e.g., Figure 1.1. ABC Festival. Source: XYZ: PQ Publishers, May 2000, p.20)

Figure 1(a), Figure 4(a),(b),(c),(d)

Factor 1: Consider the purpose and character of the use you made of someone else's copyrighted material in your ETD.

Assumptions impacting this factor: An ETD available on the Internet is considered the equivalent to making multiple copies available. VT is a non-profit educational institution. The purpose of the ETD is research, academic and educational.

1. Was the purpose of your use of the copyrighted work for a business or commercial activity?

- ○ Yes
- ◉ No

2. Was the reason for using the copyrighted work also to entertain?

- ○ Yes
- ◉ No

3. Was criticism, commentary, news reporting, or parody a reason for using the copyrighted work in your ETD?

- ○ Yes
- ◉ No

4. Have you given credit to the author or creator of the copyrighted work in your ETD?

- ◉ Yes
- ○ No

5. Did you redo or alter the copyrighted work to serve a new purpose when you used it in

your ETD?

- ○ Yes
- ◉ No

Factor 2: Consider the nature of the copyrighted work you used in your ETD.

1. Is it a creative work, such as a picture of a painting, a poem, or a work of fiction?

- ○ Yes
- ◉ No

2. Did it come from a published work?

- ◉ Yes
- ○ No
- ○ Don't know

3. Is it a factual work, such as a quote from a scientific journal, a graph or a table derived from statistical data?

- ◉ Yes
- ○ No

Factor 3: Consider the extent and significance of the copyrighted work you used.

1. Did you use a substantial portion of the copyrighted work?

- ○ Yes
- ◉ No

2. Was the part of the copyrighted work you included in your ETD a negligible part of the whole work?

- ◉ Yes
- ○ No
- ○ Don't know

3. Was the portion of the work you included in your ETD central to or the heart of the copyrighted work?

- ○ Yes
- ○ No
- ◉ Don't know

Factor 4: Consider the effect your use of the copyrighted material may have on the (potential) sale of the copyrighted work.

1. Did you lawfully acquire a copy of copyrighted material you used in your ETD?

- ◉ Yes
- ○ No

2. Will access to the copyrighted work in your ETD have a notable effect on the market

or potential market for the original work?

- ○ Yes
- ◉ No
- ○ Don't know

3. Is there a licensing mechanism in place for using the copyrighted work?

- ○ Yes
- ◉ No
- ○ Don't know

4. Could access to the copyrighted material in your ETD replace the use of original copyrighted work?

- ○ Yes
- ◉ No

5. Would it be affordable (i.e., cost-effective) for you to get permission for using the copyrighted work?

- ○ Yes
- ◉ No
- ○ Don't know

Analyze Fair Use

Draft 09/01/2009

(Questions? Concerns? Contact Gail McMillan, Director of the Digital Library and Archives at Virginia Tech's University Libraries: gailmac@vt.edu)

(Please ensure that Javascript is enabled on your browser before using this tool.)

Virginia Tech ETD Fair Use Analysis Results

This is not a replacement for professional legal advice but an effort to assist you in making a sound decision.

Name: Kapil Vitthalbhai Panchal

Description of item under review for fair use: Figure 1(a), Figure 4(a),(b),(c),(d)

Report generated on: 10-26-2011 at : 09:22:12

Based on the information you provided:

Factor 1

Your consideration of the purpose and character of your use of the copyright work weighs: ***in favor of fair use***

Factor 2

Your consideration of the nature of the copyrighted work you used weighs: ***in favor of fair use***

Factor 3

Your consideration of the amount and substantiality of your use of the copyrighted work weighs: ***in favor of fair use***

Factor 4

Your consideration of the effect or potential effect on the market after your use of the copyrighted work weighs: ***in favor of fair use***

Based on the information you provided, your use of the copyrighted work weighs: *in favor of fair use*